ELECTRICAL AND MECHANICAL PROPERTIES OF MOLECULAR JUNCTIONS AND NANO SURFACES

by

Zainelabideen Yousif Mijbil Al-Milli

Submitted in part fulfilment of the requirements for the degree of Doctor of Philosophy at Lancaster University, UK, January 2017

Declaration

Hereby, I declare that the current thesis is the personal work and efforts of the author and has not been submitted for any other higher education degree elsewhere.

The work has been carried out under the supervision of Prof. Colin J. Lambert at Lancaster University, UK for the period from July 2013 to January 2017.

Zainelabideen Y. Mijbil

Dedication

My origin, my parents,
My beloved and patient wife, Aryaf,
My lovely kids, Fatimah and Ahmed,
My dearest siblings.

Acknowledgement

Firstly and lastly, praise is for *Alla…* via *the Fourteenth* for everything.

I am speechless towards my deeply admired supervisor *Prof. Colin J. Lambert.*

Gratitude is the least word I can say to *Dr. Steven Bailey* for his time, lecture notes, discussions, codes, support, and smile.

Thanks should be gratefully paid to Dr. Iain Grace and Dr. David Zs. Manrique.

I would also be proud to thank my colleagues Dr. Oday, Alaa, Mohammed, Nasser, Dr. Ali (Khalid), Dr. Qusay, Mohsin, Dr. Laith, Dr. Amal, Marjan, Michael, Qingqing.

Special thanks to my wonderful colleagues and neighbours, Dr. Hatef Sadeghi and Dr. Sara Sangtarash for discussions, support and taking care of my son.

Sincere gratitude to my injured country IRAQ for granting me this precious scholarship.

Abstract

The behaviour of two graphene based structures has been theoretically investigated and analysed by using one or more tools. This tool kit consists firstly of SIESTA, a density functional theory software package, secondly Gollum, a non-equilibrium Green's function code, and finally the tight binding approach. The first project considers the variation of the thermoelectric properties of a graphene-graphene junction functionalised by the amino-silane molecule. The second project studies the mechanical properties of the interface between a silicon-carbide substrate and monolayer graphene. The results of these two projects are summarised in the next paragraphs.

The calculation of the thermoelectric properties of a graphene-silane-graphene junction reveals a number of interesting results. The most important result is that silane hinders the cross-plane electron transmission and thermal conductance. Such properties have effective applications through controlling the heat flow in the electronic chip. Furthermore, the silane molecule enhances the figure of merit of the junction which refers to the ability to convert heat. To sum up, silane-functionalized graphene has an improved heat mediation over a non-functionalised junction.

The second project analyses the mechanical properties of the silicon-carbide/graphene junction. The study of this junction focuses on the trends in terms of stiffness and work function as the hydrogen concentration intercalating the interface and the number of graphene sheets on top of the silicon-carbide substrate varies. As a result of this study I have found that the effect of increasing the number of penetrating hydrogen atoms is to reduce the stiffness and to enhance the work function. The same situation is found for the stiffness when the number of graphene layers is increased. However the work functions shows two completely opposing behaviours; the first one can be seen in the quasi-free standing graphene layer type 1 and type 2, where the work function has increased, while it has decreased for as-grown interface. An additional property can be deduced is that a certain amount of hydrogen atoms at the interface of approximately 33%, can dramatically change the characteristics of the interface. Another feature is that the junctions exhibit three distinct values of stiffness depending on the hydrogen concentration. The highest value is calculated for the directly attached graphene

sheet to the silicon-carbide, while the softest junction is obtained when the concentration of hydrogen atoms passivates more than 50% of the surface silicon atoms. The last value has been shown for the graphene-graphene layer.

Accomplishments

1. Haoxue Han, Yong Zhang, Nan Wang, Majid Kabiri Samani, Yuxiang Ni, Zainelabideen Y. Mijbil, Michael Edwards, Shiyun Xiong, Kimmo Sääskilahti, Murali Murugesan, Yifeng Fu, Lilei Ye, Hatef Sadeghi, Steven Bailey, Yuriy A. Kosevich, Colin J. Lambert, Johan Liu and Sebastian Volz, Functionalization mediates heat transport in graphene nanoflakes, Nature Communication, 7, 11281, 2016, DOI: 10.1038/ncomms11281.
2. N. D. Kay, C. Melios, Z. Y. Mijbil, W Strupiński, O. Kazakova, Steven W. D. Bailey, O. V. Kolosov, C. J. Lambert, Interplay between electronic and nano-mechanical properties of quasi-free standing graphene on SiC, In preparation.
3. GOLLUM team member, http://www.physics.lancs.ac.uk/gollum/index.php/about.

Contents

Chapter 1 - Introduction

Over the last two decades, condensed matter physics has witnessed great advances in both theoretical and experimental methods. These advances have enabled scientists to create new materials[1, 2], minimize the structure of electronic circuits[3, 4] and develop powerful simulation tools[5-7]. Molecular electronics has arisen as a novel field with ever expanding possibilities dating back to 1974, when the first prediction was proposed by Aviram and Ratner[8].

However reducing the size of a circuit, to nearly 10 nm or less[9] requires the development of new theories to explain and analyze the behavior of molecules in such realms or to predict their properties and phenomena[10]. The aim of this thesis is to present a step forward to deepen our understanding of molecular electronics and to therefore help strengthen the technology by suggesting new devices as our pivotal goals.

To achieve these aims an effective road map has been set up which consists of three main steps. Firstly, structure optimization via density functional theory (DFT), secondly calculating the single electron transmission via a Green's function formalism (GF) and finally to analyse the results by using the tight binding (TB) approach.

The above three steps have certain dependencies. For example the DFT calculations describe the ground state properties whereas the GF mainly depends on DFT for the transmission calculation since it requires a DFT Hamiltonian of the system[11]. In contrast to GF, TB can either be fully or partially independent from DFT.

Regarding the importance of these three theoretical tools I have devoted chapter two in this thesis to briefly discuss DFT starting from the very beginning up to current implementation in the numerical codes such as SIESTA [12] and CASTEP [13]. The next part of chapter two deals with GF in more detail as it is extensively applied and

developed by our group and can provide comprehensive information about the system. The TB approach is presented in the last section in chapter two.

The following chapters will be organized so that they illustrate the projects I have carried out using the aforementioned procedures. Chapter three illustrates the effect of single molecule on the cross plane transmission of graphene. The results can be exploited to control the heat produced in the electronic devices and then either efficiently discards the excess heat or transforms it into a power via the Seebeck effect.

Chapter four investigates the topological properties of a graphene sheet above a silicon carbide (4*H*-SiC) substrate. The workfunction, stiffness, and charge transfer for different number of layers of graphene on top of SiC were checked in addition to the calculation of the same properties as a function of hydrogen intercalating between the sheet and the substrate.

Chapter 2 - Theoretical Methods

2.1. Introduction

The main purpose I am trying to achieve is calculating the transmission coefficient of a molecular junction. From the behaviour of the transmission I can deduce very important information about the electronic nature of the system under bias, for example, conductance, power transmission efficiency, the type of charge carriers, and susceptibility to the environment. All of this data about the behavior of molecular junction has many potential applications such as transistors, sensors, rectifiers, electrodes and solar cells.. Therefore to gain the transmission amplitude I need to obtain the Hamiltonian of the system which can be acquired by solving the many-body Schrödinger equation.

However solving the Schrödinger equation for many interacting particles is a difficult task even more so for a system with thousands of atoms. Therefore I resort to approximations such as DFT. The obstacle of DFT is that it only calculates the ground state properties i.e. the properties of a closed system. This means that I cannot calculate the transmission coefficient because it is a property of an open structure which is a system which allows electrons to flow from one side of a device to another. To overcome this barrier a Green's function formalism is adopted which describes the susceptibility of any point in the whole system to the distortion in the source[14].

In summary this chapter will present

1. The method used to obtain the Hamiltonian of the system via DFT.
2. The implementation of the Hamiltonian from DFT in Green's function to calculate the transmission coefficient of the system.
3. The tight binding procedure to mimic the DFT-Hamiltonian and the GF-transmission coefficient and analyse the results.

2.2. Density Functional Theory (DFT)

The first section in the current chapter deals with DFT. Therefore, the main purpose of this section is to give a general understanding, since it is not a DFT or quantum chemistry textbook, of how this theory works and the historical developments led to the present well-known theory. Based on this I will start my DFT journey with the pretty, elegant equation of Schrödinger.

2.2.1. Many-particle Schrodinger equation

A fundamental starting point of any computational methods, whether it is DFT or not, is writing down the Schrödinger equation,

$$\hat{H} \mid \Psi\rangle = E \mid \Psi\rangle \tag{2.1}$$

$$\Psi = \Psi\left(r_1, r_2, \ldots, r_N, R_1, R_2, \ldots, R_N\right) \tag{2.2}$$

where $\hat{H}$ represents the total Hamiltonian of the system, E the corresponding eigenvalues, and Ψ is the total wave function of the system, in which the positions of the electrons and nuclei are represented by r_i and $R_{j,}$ respectively. The explicit and general form of $\hat{H}$, for a system with N_e number of electrons and N_n number of atoms, is

$$\begin{aligned}\hat{H} &= -\sum_{i=1}^{N_e}\frac{\hbar^2}{2m_e}\frac{d^2}{dr_i^2} - \sum_{j=1}^{N_n}\frac{\hbar^2}{2m_n}\frac{d^2}{dR_j^2} + \sum_{i\neq i'}^{N_e}\frac{e^2}{\left|r_i - r_{i'}\right|} + \sum_{j\neq j'}^{N_n}\frac{Z_j Z_{j'} e^2}{\left|R_j - R_{j'}\right|} + \sum_{i=1}^{N_e}\sum_{j=1}^{N_n}\frac{Z_j e^2}{\left|r_i - R_j\right|} \\ &= \hat{T}_e + \hat{T}_N + \hat{V}_{ee} + \hat{V}_{NN} + \hat{V}_{eN}\end{aligned} \tag{2.3}$$

where

$$\hat{T}_e = -\sum_{i=1}^{N_e} \frac{\hbar^2}{2m_e} \frac{d^2}{dr_i^2}; \quad \hat{V}_{ee} = \sum_{i \neq i'}^{N_e} \frac{e^2}{|r_i - r_{i'}|}; \quad \hat{V}_{eN} = \sum_{i=1}^{N_e} \sum_{j=1}^{N_n} \frac{Z_j e^2}{|r_i - R_j|}$$

$$\hat{T}_N = -\sum_{j=1}^{N_n} \frac{\hbar^2}{2m_n} \frac{d^2}{dR_j^2}; \quad \hat{V}_{NN} = \sum_{j \neq j'}^{N_n} \frac{Z_j Z_{j'} e^2}{|R_j - R_{j'}|}$$

where $\hat{T}_e$ and $\hat{T}_N$ are the kinetic energy of electrons and nuclei respectively. The electron-electron potential is represented by $\hat{V}_{ee}$, $\hat{V}_{eN}$ is the potential between electrons and nuclei, and $\hat{V}_{NN}$ represents the potential between nuclei. Suffices *i* and *j* refer to the electron and nucleus respectively. The electron charge is *e*, *Z* is the atomic charge, the reduced Planck constant is $\hbar$, and the mass of electron and nucleus are m_e and m_n respectively [15]. However, solving such an equation for large systems is a problematic task. Therefore, a number of approximations have been suggested and applied.

2.2.2. Adiabatic approximation

The first step, applied to expedite the solution of Schrödinger equation Eq.(2.3), is the adiabatic (or Born-Oppenheimer) approximation. This approximation simply ignores the kinetic energy of the nuclei. Thus, the Schrödinger Hamiltonian can be written as a sum of two Hamiltonians,

$$\hat{H} = \hat{H}^e + \hat{H}^N \tag{2.4}$$

$$\hat{H}^N = \hat{T}_N + \hat{V}_{NN} \tag{2.5}$$

$$\hat{H}^e = \hat{T}_e + \hat{V}_{ee} + \hat{V}_{eN} \tag{2.6}$$

Where $\hat{H}^N$ represents the nucleus part and $\hat{H}^e$ stands for the electron part.

The justification for this operation is that the mass of the nucleus is much greater than the mass of the electron and their movement is much slower than the electron. As a result, the electrons can simultaneously adjust themselves to the position of the nucleus[16].

2.2.3. Thomas-Fermi theory

The second step is Thomas-Fermi (TF) approximation, which is regarded as the first ancestor approach of today's well known DFT method. The beauty of the TF approach is the replacement of a vector state by a one variable scalar function, namely the electron density $n(r)$, i.e., instead of using Eq.(2.2) as a solution one can use $n(r)$. However, the TF approach adapted different calculation logic, rather than using the usual Schrödinger equation, they suggest that the energy $E_{TF}[n(r)]$ of the atom can be calculated using the following formula

$$E_{TF}[n_{TF}(r)] = C_{TF}\int dr\ \left[n_{TF}(r)\right]^{\frac{5}{3}} - Z\int dr\ \frac{n_{TF}(r)}{r} + \frac{1}{2}\int\int dr'\ dr''\ \frac{n_{TF}(r')n_{TF}(r'')}{\left|r'-r''\right|} \qquad (2.7)$$

$$n_{TF}(r) = \frac{dN_e}{dr} \qquad (2.8)$$

where C_{TF} is a constant, equal to 2.871 a.u., and r, r',and r'' are vectors defining the space of the whole system, the first electron atomic space, and second electron atomic space respectively [17].

2.2.4. The Hohenberg-Kohn Theorems

The third step, effectively contributed to the emergence of DFT, was opened by the Hohenberg-Kohn theorems, which state:

1. The system would have a unique ground state density $n_0(r)$ associated with a specific external potential v_{ext}, where $v_{ext} \equiv \hat{V}_{eN}$. It is worth to mention that the nomenclature for $\hat{V}_{ee}$ in Hohenberg-Kohn theorems is V_{int}.
2. The energy of the system $E[n_0(r)]$ associated with that external potential v_{ext} is the global minimum point and the related ground state density $n_0(r)$ is the exact solution.

The contributions of these theorems into DFT are:

1. One can divide the Hamiltonian of Eq. (2.6) into two parts: the intrinsic electronic part and the nucler part, which can be dealt with as external potential v_{ext}
2. Both the external potential and the ground state density map each other, $v_{ext} \leftrightarrow n_0(r)$.
3. The total energy of the system can be written as a functional of the ground state density $E[n_0(r)]$.

According to the above results, the total energy of the system can be written as [16],

$$\begin{aligned} E[n(r)] &= \left\langle \Psi\left[n(r)\right] \middle| \hat{T}_e \middle| \Psi\left[n(r)\right] \right\rangle + \left\langle \Psi\left[n(r)\right] \middle| \hat{V}_{ee} \middle| \Psi\left[n(r)\right] \right\rangle + \int v_{ext}(r)\, n(r)\, d^3r \\ &= T_{HK}[n(r)] + V_{HK}[n(r)] + V_{ext}[n(r)] \end{aligned} \tag{2.9}$$

where

$$\begin{aligned} T_{HK}[n(r)] &= \left\langle \Psi\left[n(r)\right] \middle| \hat{T}_e \middle| \Psi\left[n(r)\right] \right\rangle \\ V_{HK}[n(r)] &= \left\langle \Psi\left[n(r)\right] \middle| V_{ee} \middle| \Psi\left[n(r)\right] \right\rangle \\ V_{ext}[n(r)] &= \int v_{ext}(r)\, n(r)\, d^3r \end{aligned} \tag{2.10}$$

2.2.5. Kohn-Sham theorems

The final step which shaped the modern DFT is the Kohn-Sham theorems. The key idea of these theorems is the replacement of the ground state energy functional of an inhomogeneous interacting particle system with a homogeneous non-interacting one. This means that instead of solving one M-particle Schrödinger equation, one can solve M one-particle Schrödinger equations. In addition, they have explicitly introduced the exchange and correlation operator, but as yet this needs to be solved self consistently.

Kohn-Sham starting point is [18],

$$E_{non}[n(r)] = T_{non}[n(r)] + V_{HK}[n(r)] + V_{ext}(r) + V_{xc}[n(r)] \tag{2.11}$$

where T_{non} is the kinetic energy of a non-interacting-particle system, and V_{XC} is the exchange-correlation energy of the interacting-particle system.

As a result of minimizing Eq. (2.11), Kohn-Sham were able to suggest the following:

The equations govern the interacting particle system are exactly as the same as the non-interacting particle system under a specific potential. Thus, self-consistently solving a Schrodinger one-particle equation (Eq. (2.12)) of non-interacting-particle system to obtain the required potential is equivalent to that of interacting system[19].

$$\left\{ -\frac{\hbar^2}{2m_e}\nabla^2 + v_{ext}(r) + \int dr \ \frac{n(r')}{|r-r'|} + \frac{d}{dn}n(r) \ v_{xc}[n(r)] \right\} \psi_i(r) = \varepsilon_i \ \psi_i(r) \tag{2.12}$$

$$n(r) = \sum_{i}^{N_e} |\psi_i(r)|^2 \tag{2.13}$$

The trick is that after obtaining the density $n(r)$, one should define the potentials in (2.11). The next step is to minimize (2.11) in order to solve (2.12), i.e., a self-consistent iteration[18].

2.2.6. Exchange and correlation potential

Even though Kohn-Sham had introduced the term exchange-correlation potential, they did not define it exactly. Therefore, as a rule of thumb, the absence of an optimum and comprehensive exchange-correlation (XC) functional definition should be confirmed, and all methods should be calibrated with pretested results[20]. Bearing this in mind, one should start from the general definition of the exchange-correlation energy, which is the difference between the energy of inhomogeneous interacting electron system and the energy of homogeneous non-interacting electron system. Although, this difference can exactly be calculated numerically via a *number* of contributions, but in real life I have to apply approximations, which defines the margin that all XC approximations work within[21, 22].

For instance the local density approximation (LDA) is the first XC approach proposed by Kohn and Sham in 1965. They suggested a solution to $V_{xc}[n(r)]$ in Eq. (2.11) as,

$$V_{xc}[n(r)] = \int dr\; n(r)\; v_{xc}[n(r)] \tag{2.14}$$

where $v_{xc}[n(r)]$ is the electron exchange-correlation in the homogeneous electron gas. LDA is valid, provided that the density $n(r)$ is highly localized with slow variation.

Now by subjecting Eq. (2.11) to

$$\int \delta n(r)\; dr = 0 \tag{2.15}$$

$$\int \delta n(r) \left\{ \epsilon_{int}[n(r)] + \frac{\delta T_{non}[n(r)]}{\delta n(r)} + \epsilon_{xc}[n(r)]) \right\} dr = 0 \tag{2.16}$$

$$\epsilon_{xc}[n(r)] = \frac{d}{dn} n(r)\; v_{xc}[n(r)] \tag{2.17}$$

$$\epsilon_{int}[n(r)] = v_{ext}(r) + \int dr' \frac{n(r')}{|r - r'|} \tag{2.18}$$

Kohn-Sham have separated the potentials into two terms, where Eq. (2.17) depicts the exchange-correlation participation, and the left potential represent the internal potential, Eq. (2.18) [18].

2.2.7. SIESTA

DFT electronic structure calculations have been performed by using SIESTA, Spanish Initiative for Electronic Simulations with Thousands of Atoms. SIESTA produces the ground state properties and the mean field Hamiltonian, which is the main requirement to perform the transport calculations [12, 23]. The main features of SIESTA can be summarised as,

- Linear scaling DFT method [7, 24].
- Implementation of Linear Combination of Atomic Orbitals (LCAO) via using numerical atomic orbitals basis sets [25].
- Eliminating core electrons through Kleinman-Bylander approach for norm-conserving pseudopotential [26].
- Hellmann-Feynman theory has been used for forces between atoms [23].

2.3. Green's Function (GF)

The first section of this chapter briefly reviewed how DFT can be used to obtain the Hamiltonian of the system. In this section I will demonstrate the way to use the DFT mean field Hamiltonian (DFT-mfH) via Green's function method to calculate the transmission coefficient $\tau(E)$ [27, 28]. Therefore the GF's procedures followed to calculate $\tau(E)$ are

1. Calculating the GF of double infinite periodic lead.
2. Calculating surface GF of the lead via applying boundary conditions.

3. Using Dyson's equation to obtain the total Green's function of the whole system, i.e., a system with two leads plus scatter region.
4. Calculating the τ(E) of the electron from one lead to the other through the molecule.

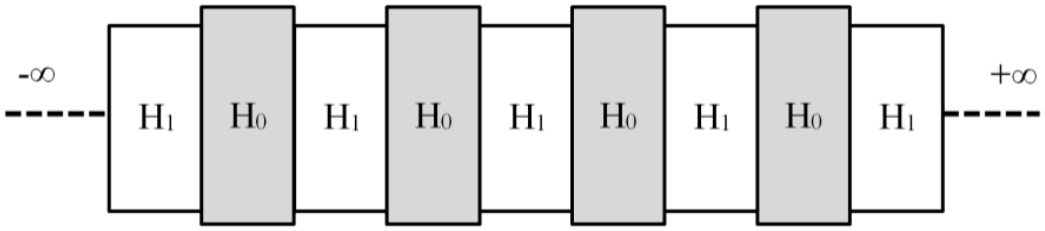

Figure 1: Double infinite lead with H0 Hamiltonian for the interactions within a single layer and H_1 Hamiltonian to represent the interactions between two adjacent layers.

2.3.1. Mean field Hamiltonian

The starting point is the Hamiltonian of the system, which can mainly be divided into two parts; the semi-infinite lead parts and the scattering region (SR) part. This procedure makes life easy and also takes into account the effect of the leads on the scattering region without losing generality [27]. As a result, I can now deal with the Hamiltonian of the leads without worrying about the SR. In addition to the first separation between Hamiltonians, I can also deconstruct the total Hamiltonian of the double infinite lead into two parts as well, so that it will be a combination of perfectly periodic layers along the transport direction, which is usually the *z* direction as shown in Figure 1. Each layer is described by a sub-Hamiltonian H_0 which includes orbital interactions within a single

layer and another sub-Hamiltonian H_1 describing the orbital interactions between two adjacent layers. I can then write down the Hamiltonian of double infinite lead as,

$$H = \begin{bmatrix} \ddots & H_1 & 0 & 0 & 0 \\ H_1^\dagger & H_0 & H_1 & 0 & 0 \\ 0 & H_1^\dagger & H_0 & H_1 & 0 \\ 0 & 0 & H_1^\dagger & H_0 & H_1 \\ 0 & 0 & 0 & H_1^\dagger & \ddots \end{bmatrix} \tag{2.19}$$

Therefore, the Schrödinger equation can be written as,

$$H_0\psi_j + H_1^\dagger\psi_{j-1} + H_1\psi_{j+1} = E\psi_j \tag{2.20}$$

Since I have an infinitely periodic system along the *z* direction and finite in the other directions, I can apply Bloch's theorem for the wave function, such that,

$$\psi_j = A_k e^{ikj}\varphi_k \tag{2.21}$$

where *k* represents the wavenumber and A_k is the normalization constant. By substituting this result into Eq. (2.20) and do simple mathematical manipulations, I will have the dispersion relation of the system by solving secular equation which results in the following determinant equation,

$$\det(H_0 + H_1 e^{ik} + H_1^\dagger e^{-ik} - E) = 0 \tag{2.22}$$

Equation (2.20) can be also rewritten to be in a numerical friendly form,

$$\begin{pmatrix} H_1^{-1}(E - H_0) & H_1^{-1}H_1^\dagger \\ I & 0 \end{pmatrix}\begin{pmatrix} \varphi_k \\ \mu_k \end{pmatrix} = e^{ik}\begin{pmatrix} \varphi_k \\ \mu_k \end{pmatrix} \tag{2.23}$$

where $\mu_k = e^{-ik}\varphi_k$. The last two equations give rise to the following important results:

1. From Eq. (2.22), the number of the bands (*M*) is equal to the number of orbitals in H_0.
2. Symmetric bands can be seen if the H_1 is hermitian, while asymmetric bands when H_1 is not hermitian.

3. Positive (negative) real values of *k* result in right (left) propagating modes, with a positive (negative) group velocity (v), which is associated with an open channel.

$$v = \frac{1}{\hbar}\partial_k E(k) \tag{2.24}$$

4. Positive (negative) complex values of *k* result in right (left) decaying mode, i.e. closed channels.

2.3.2. Green's function of double infinite lead (DIL)

Based on the solution for the wave function of the double infinite lead a Green's Function can be constructed as,

$$g_{j,j'}^{DIL} = \begin{cases} \left|\varphi_k\right\rangle e_k \left\langle B_k\right| & j \geq j' \\ \left|\varphi_{\bar{k}}\right\rangle e_{\bar{k}} \left\langle B_{\bar{k}}\right| & j' \leq j \end{cases} \tag{2.25}$$

where

$$\begin{aligned} \left|\varphi_k\right\rangle e_k \left\langle B_k\right| &= \sum_v^M \varphi_{k_v} e^{ik_v(j-j')} B_{k_v} \\ \left|\varphi_{\bar{k}}\right\rangle e_{\bar{k}} \left\langle B_{\bar{k}}\right| &= \sum_v^M \varphi_{\bar{k}_v} e^{i\bar{k}_v(j-j')} B_{\bar{k}_v} \end{aligned} \tag{2.26}$$

The first and second parts of Eq. (2.25) represent a distortion propagating to the right and left of the source at point *j´*, respectively. This means a retarded Green's Function construction. Thus, for $g_{j,j'}$ to be a solution, it should fulfill two conditions:

1. It should be continuous at *j=j´*.

$$\left|\varphi_k\right\rangle\left\langle B_k\right| = \left|\varphi_{\bar{k}}\right\rangle\left\langle B_{\bar{k}}\right| \tag{2.27}$$

2. Should fulfill Green's Function equation,

$$(E-H)G=I, \tag{2.28}$$

which gives

$$H_1^{\dagger}\left(\left|\varphi_{\bar{k}}\right\rangle e_{\bar{k}}\left\langle B_{\bar{k}}\right|-\left|\varphi_k\right\rangle e_k\left\langle B\right|\right)=I \tag{2.29}$$

Introducing the dual space theorem,

$$\left|\varphi_k\right\rangle\left\langle\varphi_k\right|=\left|\varphi_{\bar{k}}\right\rangle\left\langle\varphi_{\bar{k}}\right|=I \tag{2.30}$$

Therefore

$$\begin{aligned}\left\langle B_k\right|&=\left\langle\varphi_k\left|\varphi_{\bar{k}}\right\rangle\right\langle B_{\bar{k}}\right|\\ \left\langle B_{\bar{k}}\right|&=\left\langle\varphi_{\bar{k}}\left|\varphi_k\right\rangle\right\langle B_k\right|\end{aligned} \tag{2.31}$$

Plugging the last result into Eq. (2.29) and using the continuity equation, Eq. (2.27), I obtain

$$\begin{aligned}H_1^{\dagger}\left\{\ \left(\left|\varphi_{\bar{k}}\right\rangle e_{\bar{k}}\left\langle\varphi_{\bar{k}}\left|\varphi_k\right\rangle\right\langle B_k\right|\right)-\left(\left|\varphi_k\right\rangle e_k\left\langle\varphi_k\left|\varphi_{\bar{k}}\right\rangle\right\langle B_{\bar{k}}\right|\right)\ \right\}&=I\\ H_1^{\dagger}\left\{\ \left(\left|\varphi_{\bar{k}}\right\rangle e_{\bar{k}}\left\langle\varphi_{\bar{k}}\left|\varphi_{\bar{k}}\right\rangle\right\langle B_{\bar{k}}\right|\right)-\left(\left|\varphi_k\right\rangle e_k\left\langle\varphi_k\left|\varphi_{\bar{k}}\right\rangle\right\langle B_{\bar{k}}\right|\right)\ \right\}&=I\\ H_1^{\dagger}\left\{\ \left(\left|\varphi_{\bar{k}}\right\rangle e_{\bar{k}}\left\langle\varphi_{\bar{k}}\right|\right)-\left(\left|\varphi_k\right\rangle e_k\left\langle\varphi_k\right|\right)\ \right\}\ \left|\varphi_{\bar{k}}\right\rangle\left\langle B_{\bar{k}}\right|&=I\\ \left\langle\varphi_{\bar{k}}\right|C^{-1}&=\left\langle B_{\bar{k}}\right|\end{aligned} \tag{2.32}$$

where

$$C = H_1^{\dagger}\left\{ \left(\left|\varphi_{\bar{k}}\right\rangle e_{\bar{k}} \left\langle\varphi_{\bar{k}}\right|\right) - \left(\left|\varphi_k\right\rangle e_k \left\langle\varphi_k\right|\right) \right\} \tag{2.33}$$

$$g_{j,j'}^{DIL} = \begin{cases} \left|\varphi_k\right\rangle e_k \left\langle\varphi_k\right| C^{-1} & j \geq j' \\ \left|\varphi_{\bar{k}}\right\rangle e_{\bar{k}} \left\langle\varphi_{\bar{k}}\right| C^{-1} & j' \leq j \end{cases} \tag{2.34}$$

2.3.3. Surface Green's function (SGF)

I obtain the SGF by applying boundary conditions into the double infinite lead GF via adding a new wave function. This procedure constructs a new Green's Function for a semi-infinite lead (SIL), by which the left and right leads will extend until $j=j_0$, i.e. I can define the left lead to be periodic within $(-\infty, j_0-1)$ and the right lead within (j_0+1, ∞). Thus

$$g_{j_0,j_0}^{L} = g_{j_0,j_0}^{R} = 0 \tag{2.35}$$

and

$$g_{j,j'}^{SIL} = \begin{cases} g_{j,j'}^{DIL} + \psi_{j',j_0}^{L} & j' \geq j \\ g_{j,j'}^{DIL} + \psi_{j',j_0}^{R} & j \geq j' \end{cases} \tag{2.36}$$

$$\psi_{j',j_0} = \begin{cases} \left|\varphi_{\bar{k}}\right\rangle e^{i\bar{k}j} D^{(L)} & j' \geq j \\ \left|\varphi_k\right\rangle e^{ikj} D^{(R)} & j \geq j' \end{cases} \tag{2.37}$$

Substituting (2.37) into (2.36) and using the result of (2.35), I can define D for the left and right propagating waves as,

$$D=\begin{cases} -e^{-i\bar{k}j_0}\left\langle \varphi_{\bar{k}}\middle|\varphi_k\right\rangle e^{ik(j_0-j)}\left\langle \varphi_k\middle|C^{-1}\right. & j'\geq j \\ -e^{-ikj_0}\left\langle \varphi_k\middle|\varphi_{\bar{k}}\right\rangle e^{i\bar{k}(j_0-j)}\left\langle \varphi_{\bar{k}}\middle|C^{-1}\right. & j\geq j' \end{cases} \tag{2.38}$$

Thus, the semi-infinite lead Green's function,

$$g_{j,j'}^{SIL}=\begin{cases} \left[\left|\varphi_k\right\rangle e_k\left\langle \varphi_k\middle|-\middle|\varphi_{\bar{k}}\right\rangle e^{i\bar{k}j}-e^{-i\bar{k}j_0}\left\langle \varphi_{\bar{k}}\middle|\varphi_k\right\rangle e^{ik(j_0-j)}\left\langle \varphi_k\right|\right]C^{-1} & j'\geq j \\ \left[\left|\varphi_{\bar{k}}\right\rangle e_{\bar{k}}\left\langle \varphi_{\bar{k}}\middle|-\middle|\varphi_k\right\rangle e^{ikj}-e^{-ikj_0}\left\langle \varphi_k\middle|\varphi_{\bar{k}}\right\rangle e^{i\bar{k}(j_0-j)}\left\langle \varphi_{\bar{k}}\right|\right]C^{-1} & j\geq j' \end{cases} \tag{2.39}$$

Finally, I obtain the SGF as,

$$\begin{aligned} g_L^S &= g_{j_0-1,j_0-1}^{SIL}=\left[I-\left|\varphi_{\bar{k}}\right\rangle e^{-i\bar{k}}\left\langle \varphi_{\bar{k}}\middle|\varphi_k\right\rangle e^{ik}\left\langle \varphi_k\right|\right]C^{-1} \\ g_R^S &= g_{j_0+1,j_0+1}^{SIL}=\left[I-\left|\varphi_k\right\rangle e^{ik}\left\langle \varphi_k\middle|\varphi_{\bar{k}}\right\rangle e^{-i\bar{k}}\left\langle \varphi_{\bar{k}}\right|\right]C^{-1} \end{aligned} \tag{2.40}$$

2.3.4. Total Green's function (G)

As shown in Fig. (1), I can get the total Green's Function using Dyson equation [11],

$$G=(g^{-1}-H)^{-1} \tag{2.41}$$

$$g=\left(\begin{array}{ccccc:c} g_{L1}^S & 0 & 0 & 0 & 0 & \\ 0 & g_{L2}^S & 0 & 0 & 0 & \\ 0 & 0 & \ddots & 0 & 0 & \\ 0 & 0 & 0 & g_{nL}^S & 0 & \\ \hdashline 0 & 0 & 0 & 0 & g_{SR}^{iso} & \end{array}\right)_{(nL+1)\times(nL+1)} \tag{2.42}$$

$$H = \left(\begin{array}{cccc:c} 0 & 0 & 0 & 0 & H_{1SR} \\ 0 & 0 & 0 & 0 & H_{2SR} \\ 0 & 0 & 0 & 0 & \vdots \\ 0 & 0 & 0 & 0 & H_{nLSR} \\ \hdashline H_{1SR}^{\dagger} & H_{2SR}^{\dagger} & \cdots & H_{nLSR}^{\dagger} & 0 \end{array}\right)_{(nL+1)\times(nL+1)} \tag{2.43}$$

2.3.5. Transmission via Fisher-Lee

Without resorting to complicated jargon, the Fisher-Lee relation simply extracts the amplitudes of wave functions projected on scattering region from the TGF depending on two logical foundations:

1. The well-defined scattering matrix approach. Since I have coherent transport, the projected de Broglie wave of electron can either be reflected or transmitted at specific points in the system, as shown in Figure 2.
2. The "beloved" Green's Function approach. The beauty of GF is that it reveals how different parts of the system interact with each other from each matrix element. Thus I can relate the TGF element at a specific site with its counterpart amplitude to deduce the required information.

Showing how to obtain the $\tau(E)$, I will consider the simplest case where the points are on the surfaces of the leads and the transmission occurs as the electron pass from channel *i* in the first lead to channel *j* in the second lead. Therefore, the transmission amplitude (t) can be written as,

$$\begin{aligned} G_{j,i} &= t'_{j,i} \left|\varphi_{k_j}\right\rangle \left\langle\varphi_{k_i}\right| C^{-1} \\ t'_{j,i} &= \left\langle\varphi_{k_j}\right| G_{j,i} C \left|\varphi_{k_i}\right\rangle \end{aligned} \tag{2.44}$$

Where I have applied (2.34) into (2.44) to define t, and finally calculate $\tau(E)$[29]

$$t_{j,i} = t'_{j,i}\sqrt{\frac{v_j}{v_i}} \tag{2.45}$$

$$\tau(E) = \left|t_{j,i}\right|^2 \tag{2.46}$$

2.4. Tight binding (TB)

In the last two main sections, I have demonstrated how to first construct a Hamiltonian operator, via DFT, and secondly how to use this operator to calculate the transmission coefficient, via GF. Besides DFT, a number of methods are available which can fulfill the same task, of course with different accuracy. One of these methods is the Tight Binding method. The elegancy of the TB is the localization of the potentials and the wavefunctions, presumed to be orthonormal, are centered on the atomic sites [30]. These properties essentially result in a parameter dependent Hamiltonian, i.e., a few parameters, two at least, can define the whole system[31]. Furthermore, these parameters can be extracted through fitting to empirical, semi-empirical, DFT, or ansatz calculations [30]. In addition to the simplicity, TB is a very effective tool to explain and analyse the behaviour of materials[32].

Thus, Eq. (2.1) can be written as,

$$\left(E - \hat{H}\right)\left|\Psi\right\rangle = 0 \tag{2.47}$$

$$\begin{pmatrix} \ddots & \ddots & 0 & 0 & 0 & 0 & 0 \\ \ddots & \alpha & 1 & 0 & 0 & 0 & 0 \\ 0 & 1 & \alpha & 1 & 0 & 0 & 0 \\ 0 & 0 & 1 & \alpha & 1 & 0 & 0 \\ 0 & 0 & 0 & 1 & \alpha & 1 & 0 \\ 0 & 0 & 0 & 0 & 1 & \alpha & \ddots \\ 0 & 0 & 0 & 0 & 0 & \ddots & \ddots \end{pmatrix} \left|\Psi\right\rangle = 0 \tag{2.48}$$

where α is equal to $(\varepsilon_0\text{-}E)/\gamma$, ε_0 is the energy of the atomic orbital when the corresponding atom is isolated, it is also known as Coulomb integral and defined as in Eq.(2.49). The γ, defined in Eq.(2.50), is the interaction energy between two adjacent orbitals, known as resonance, tunneling or hopping integral and it measures the probability of electron i being in the orbital $\psi_j(r)$. Since the system has the property of high localization, then any interaction with remote orbitals would be very weak and can be neglected. As a result the Hamiltonian of the system in TB formula is tridiagonal matrix, as seen in Eq.(2.48).

$$\varepsilon_0 = \langle \psi_i | H | \psi_i \rangle \tag{2.49}$$

$$\gamma = \langle \psi_i | H | \psi_j \rangle \tag{2.50}$$

where ψ_i is electronic orbital centered around atom i, and ψ_j is electronic orbital at site j.

The transmission coefficient can be extracted from the TB Hamiltonian via GF the same way it is extracted from DFT one.

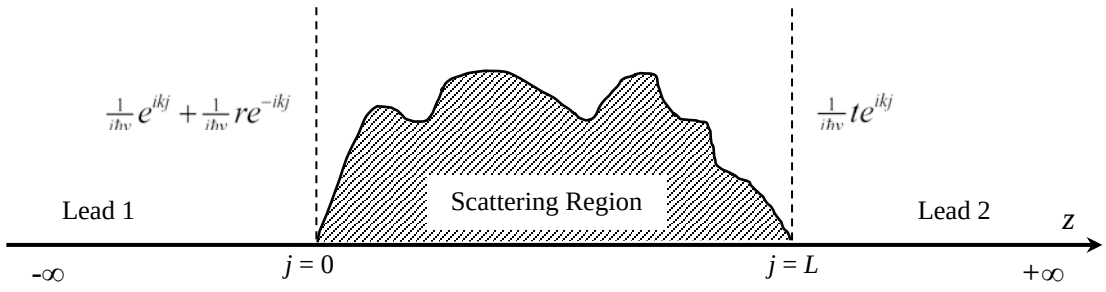

Figure 2: A schematic illustration of a 1D scattering region attached to two leads along z-direction. The points j=0 and j=L are the boundaries of the scattering region where it is attached to lead one and two respectively.

Chapter 3 - Functionalization mediates heat transport in graphene

Published in Nature Communication, 7, 11281, 2016, DOI: 10.1038/ncomms11281.

3.1. Introduction

Anisotropic properties of two-dimensional (2D) layered materials make them promising in the application of next-generation electronic devices, among which graphene and few-layer graphene (FLG) have been most intensively studied for thermal management, due to their extraordinarily high in-plane thermal conductivity (σ) [33-37]. For instance, Yan et al. [38] reported that the maximum hotspot temperature can be lowered by ~20^{o}C in transistors operating at ~13 Wmm^{-1} using FLG as a heat spreader for a gallium nitride (GaN) transistor. Gao et al. [39] reported that the maximum hotspot temperature decreased from 121 to 108^{o}C (ΔT=13^{o} C) for a heat flux of 430 W cm^{-2} after the introduction of a single-layer graphene heat spreader. Moreover, the simulations of graphene heat preaders were also reported for silicon-on-insulator integrated circuits [40] and three-dimensional (3D) integrated circuits[41]. The thermal conductivity of a graphene laminate film supported on substrate was also investigated and found to remain rather large[42]. However, in most practical applications, graphene/FLG will be supported by and integrated with insulators, both in electronic circuitry and heat-spreader applications[43]. Therefore, thermal energy flow will be limited both by the in-plane thermal conductivity (σ) of the supported graphene/FLG and by the thermal boundary resistance (R) at the graphene/FLG–substrate interface [44].

The properties of 2D layered materials are very sensitive to the interactions with external bodies. Indeed, when supported on an amorphous substrate, σ of suspended graphene decreased by almost one order of magnitude, from ~4,000 (ref.[45]) to ~600 W m^{-1} K^{-1}

(ref.[46]). Such a striking discrepancy in σ significantly limits the thermal performance of graphene/FLG in real applications. It is reported that the different behaviours are due to the strong correlation [47] to the substrate [48]. These studies have improved our fundamental understanding in the physics behind the problem, and it was suggested that making rational choice of the substrate material [46, 49] and modulating its coupling to graphene[50] may be useful to improve σ of the supported graphene/FLG.

The thermal boundary resistance (R) of a graphene/FLG–substrate interface is another limiting factor to their thermal performance in devices. Covalent functionalization has been proved to efficiently promote heat transfer between interfaces by introducing additional thermal pathways through the functionalizing molecules [51-66]. For example, self-assembled monolayers (SAMs) were used to functionalize metallic surfaces to enhance heat transport across metal–water [53, 60], metal–gas [61], metal–semiconductor [54] and metal–polymer [64] interfaces. Functionalization was used in graphene and carbon nanotube nanocomposites to mitigate the high thermal boundary resistance between the graphene/carbon nanotube fillers and the polymer matrices [51, 58, 59, 63]. Functionalized molecules also assist to align and densely pack multilayer graphene sheets and reduce the interlayer thermal resistance of graphene [58]. Recently, it was shown that plasma functionalized graphene raised the cross-plane thermal conductance between aluminum and its substrate by a factor of two[52]. Nevertheless, the functionalization-introduced point defects will further decrease σ of the supported graphene/FLG, as they introduce phonon-scattering centres [58, 65, 66]. To correct this drawback, a robust solution that maintains the high thermal conductivity of graphene/FLG when supported, while effectively reducing the interface thermal resistance is needed.

DFT calculations show that the electronic part of inter-plane thermal conductance κ_e of silane functionalized graphene can be effectively reduced due to stiffness of the amino-silane molecule which suppresses the flow of the electrons and phonons through it. Furthermore, the cross-plane thermal conductance due to phonons κ_{ph} has also decreased due to silane molecule which confirmed by the collaborating theoretician group who calculate the phonon part of thermal conductance and the experimentalist group who did

the measurements. They also verified the improvement of the in-plane thermal conductance which provides a very attractive platform for thermal management applications.

3.2. Methods

Ab initio calculations were carried out using the quantum chemistry DFT code SIESTA [12]. Local density approximations (LDA) within Ceperley-Alder version (CA), double-zeta polarized basis set, 0.01 eV/A^o force tolerance and 250 Ry mesh cutoff were all applied to obtain the relaxed atomic structures which can be seen in Figure 4-Figure 4).

First the structures were individually relaxed, where silane molecule has been kept fully isolated using 15 A^o of the vacuum region in each direction to prevent any interactions with its replica as applied in SIESTA via the supercell approach[7] to keep the periodicity of the system in three dimensions [67]. To preserve the periodicity of graphene, its geometries were kept periodic in *xy* plane and "isolated" in *z* direction.

After the relaxation of the individual systems, I sandwiched the silane molecule between two graphene monolayers to create the junction shown in Figure 4. Then and to retain a more realistic conformation, I have relaxed the junction once more following the same boundary conditions used for the graphene sheet relaxation. Next, an additional graphene layer was attached to each previously relaxed layer of the initial structure to simulate a few layers graphene junction, as shown in Figure 5a and Figure 5b.

As a reminder, it is mentioned in chapter 1 that in order to calculate the transmission coefficient of a molecule, one needs to calculate the total Green's function which depends on the Green's function of the lead. This entails creating a graphene lead which consists of four adjacent monolayers at least. Each layer should contain 90 carbon atoms to ensure there is no interaction between the silane molecule and its replicated images. This means that I need to use ~ 850 atoms to simulate the junction, which is an expensive calculation in terms of resources and time. Therefore, I redesign the model using the configuration shown in Figure 5. However, using Z-like structure immediately

creates a problem of the dangling bonds at the edges, which can be mitigated by hydrogen saturation [68].

After structure optimization, one can calculate the transmission coefficient and then thermoelectric properties. These properties can be calculated and studied via the relation between the electrical (I_e) and heat (I_q) currents on one hand and the voltage bias (ΔV) and temperature difference (ΔT) on the other hand, which is

$$\begin{pmatrix} \Delta V \\ I_q \end{pmatrix} = \begin{pmatrix} R & S \\ \Pi & \kappa \end{pmatrix} \begin{pmatrix} I_e \\ \Delta T \end{pmatrix} \tag{3.1}$$

The coefficients are: the electrical resistance R, Seebeck coefficient S, Peltier coefficient Π, and the electrical part of the thermal conductance κ_e [69]. In the linear response region of temperature and voltage, these coefficients can be calculated by [69-72],

$$G = \frac{2e^2}{h} L_0 \tag{3.2}$$

$$\kappa_e = \frac{2}{hT}\left(L_2 - \frac{L_1^2}{L_0} \right) \tag{3.3}$$

$$S = -\frac{1}{eT}\frac{L_1}{L_0} \tag{3.4}$$

$$ZT = \frac{L_1^2}{L_0 L_2 - L_1^2} \tag{3.5}$$

where

$$L_n = \int_{-\infty}^{\infty} dE \ \left(E - E_F\right)^n \ \tau(E) \ \frac{\partial f(E)}{\partial E} \tag{3.6}$$

where n is integer (= 0, 1, and 2), T is temperature, h is Plank's constant, and $f(E)$ is Fermi function, details of the derivation of the last five equations can be found in references [70, 73-75], where one can find a basic and nice derivation in the second and the third references, whereas the first and the forth references give more advanced details.

The definition for κ_e is the ratio of the heat current with respect to temperature difference between the electrodes when electrical current is zero. Similarly, Seebeck coefficient (S) is defined as the variation of the voltage ue to the temperature change in the electrodes when the electrical current is zero. Whereas, the definition for Π is the heat current induced via electrical current when the temperature difference is zero. Device efficiency to generate current due to heat transfer and vice versa is defined by the thermoelectric figure of merit (ZT) [76], which can be defined as [77],

$$ZT = \frac{S^2 G T}{\kappa}, \tag{3.7}$$

where κ = κe+κph, κph is the phonon contribution to the total thermal conductance which is calculated by the collaborative group. The phonon thermal conductance is an expensive calculation and I did not have the adequate resources to fully conduct then.

The electrical conductance G is related to the thermal conductance via Wiedemann–Franz law [36],

$$\kappa_e = \frac{\pi^2 k_B^2}{3e^2} G\ T, \tag{3.8}$$

and the Seebeck coefficient can be written in terms of energy as[78, 79],

$$S(E_F) = \frac{\pi^2 k_B^2 \overline{T}}{3e}\ \partial_{E_F} \ln \tau(E_F), \tag{3.9}$$

where $\overline{T} = (T_1 - T_2)/2$, is the leads average temperature.

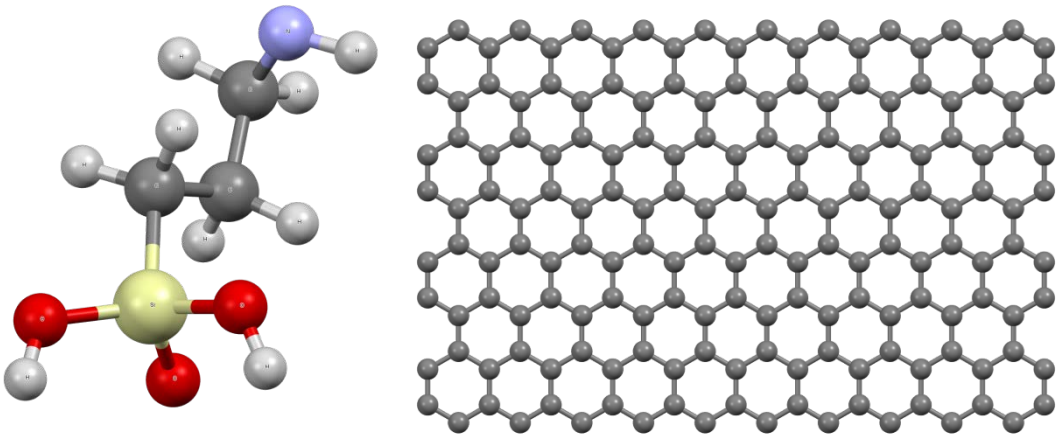

(a) (b)

Figure 4: (a) Molecular structure of silane molecule. (b) Sample of graphene sheet. The nitrogen, hydrogen, carbon, silicon, and oxygen atoms are respectively represented blue, white, gray, yellow, and red.

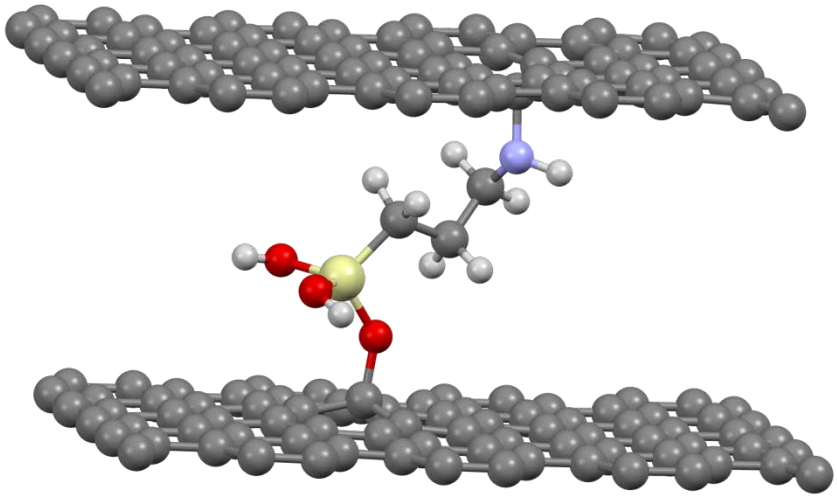

Figure 4: A representation of the graphene-silane-graphene junction, which is one part of a salf-assamble-molecule (SAM) structure. To preserve the periodicity of this structure in two dimenstions, the edges of the graphene sheets kept unsaturated to let them interact with their supercell images.

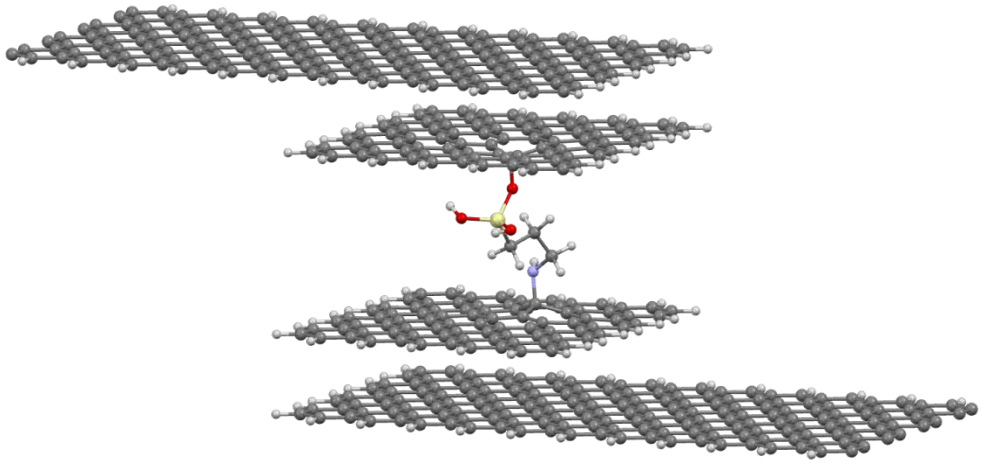

Figure 5: Graphene-silane-graphene junction, where the directly attached graphene layers have been replaced by graphene flakes because of the high expense of the calculation. For the same reason, the edges have been saturated with hydrogen. Finally, carbon and hydrogen atoms are represented by grey and white balls, the red, blue and green one are the oxygen, nitrogen, silicon atoms respectively.

Table 1: Mullikan atomic population of graphene carbon atoms attached directly to silane molecule on the right and the same atoms when silane is absence on the left hand side.

Without silane			With silane		
Atom	Mullikan Population	Δ %	Atom	Mullikan Population	Δ %
C	4.001	0.025	C	4.009	0.225
C	3.998	0.05	C	4.011	0.275
C	4.002	0.05	C	4.012	0.3
C	4.002	0.05	C	3.957	1.075
C	3.999	0.025	C	4.022	0.55
C	4.002	0.05	C	4.019	0.475
C	3.999	0.025	C	4.023	0.575
C	3.998	0.05	C	4.021	0.525
			O	6.271	4.516
			N	4.905	1.9

$\Delta=100|(A_v- M_v)/A_v|$, where A_v and M_v are the atomic and molecular valence number, respectively. Av is the valance charge of the atom in the isolated state, whereas Mv is the valnce charge of the same type of atom interacted with other atoms in the molecule. Δ represents the strength of the net transferred charge at each atom.

3.3. Results and discussion

The results can be seen in Figure 7-Figure 13, where one can notice that silane molecule has lowered $\tau(E)$, κ_e, G, Π, and S with one exception the ZT which has increased.

The first point I am going to discuss is the behaviour of the transmission coefficient, as shown in Figure 7. One can see that silane molecule has increased the distance between the graphene layers from 3.56 A^o to 8.186 A^o which destroys the long range Coulomb interaction (CI) that couples the epilayers[80] since these interactions are distance dependent[81]. In addition to the Coulomb potentials, the van der Waals (vdW) forces which interact between the adjacent layers owing to the dipole-dipole correlation of the two neutral layers are also distance dependent[80]. As a result, the interaction between two graphene monolayers is mainly defined by the distance between the layer and their charge distribution.

Graphene charge distribution can be considerably modified by nitrogen and oxygen atoms of the silane, which can also alter the bonding structure. Indeed, the nitrogen and oxygen atoms change the sp^2 into sp^3 bonding, which can be seen in the charge modulation of the interacted atoms Table 1. In the absence of silane, the sp^2 bonding is obvious where each carbon atom preserves four valence electrons. However, these carbon atom shows charge transfer in the presence of silane molecule, which means a distortion of the sp^2 bonding. Moreover, the bond lengths of these interacted carbon atoms with silane have increased confirming the sp^3 bonding[82].

Owing to elongation of the graphene interdistance and charge redistribution, asymmetric junction between the two graphene monolayer occurs in the presence of silane. This asymmetry property will decrease the transmission coefficient through the junction due the descending k values as it is approved theoretically[83] and experimentally[84]. Andres *et al.* have also mention this behaviour reporting that increasing the distance between two *AA* stacked graphene layers will change their

behaviour from metal to semimetal. They attributed this transition in the behavior to the strength of the interaction between layer. In other words, when the distance between bilayer graphene is reduced, due to stress, to be less that the van der Waals limit the bands broaden and density of states increase at K point [82].

A transmission coefficient from a tight binding toy model, shown in Figure 8, captures the main features of the transmission curve calculated by DFT which confirms the findings. In the tight binding model, the graphene sheets have been replaced by one dimension one-orbital chain, and silane molecule has been replaced by one atom intercalating the two chains, as shown in Figure 6. In Figure 8, it is worthy of note that the blue curve, system (b) in Figure 6, has a minimum at the centre of the energy domain referring to the depletion of the density of state in this point where it can be considered as a semi-metal behaviour. In contrast to the blue curve, the black one, system (a) in Figure 6, shows a high transmission peak at the same point, i.e. high density of states, which reflects a metallic behaviuor.

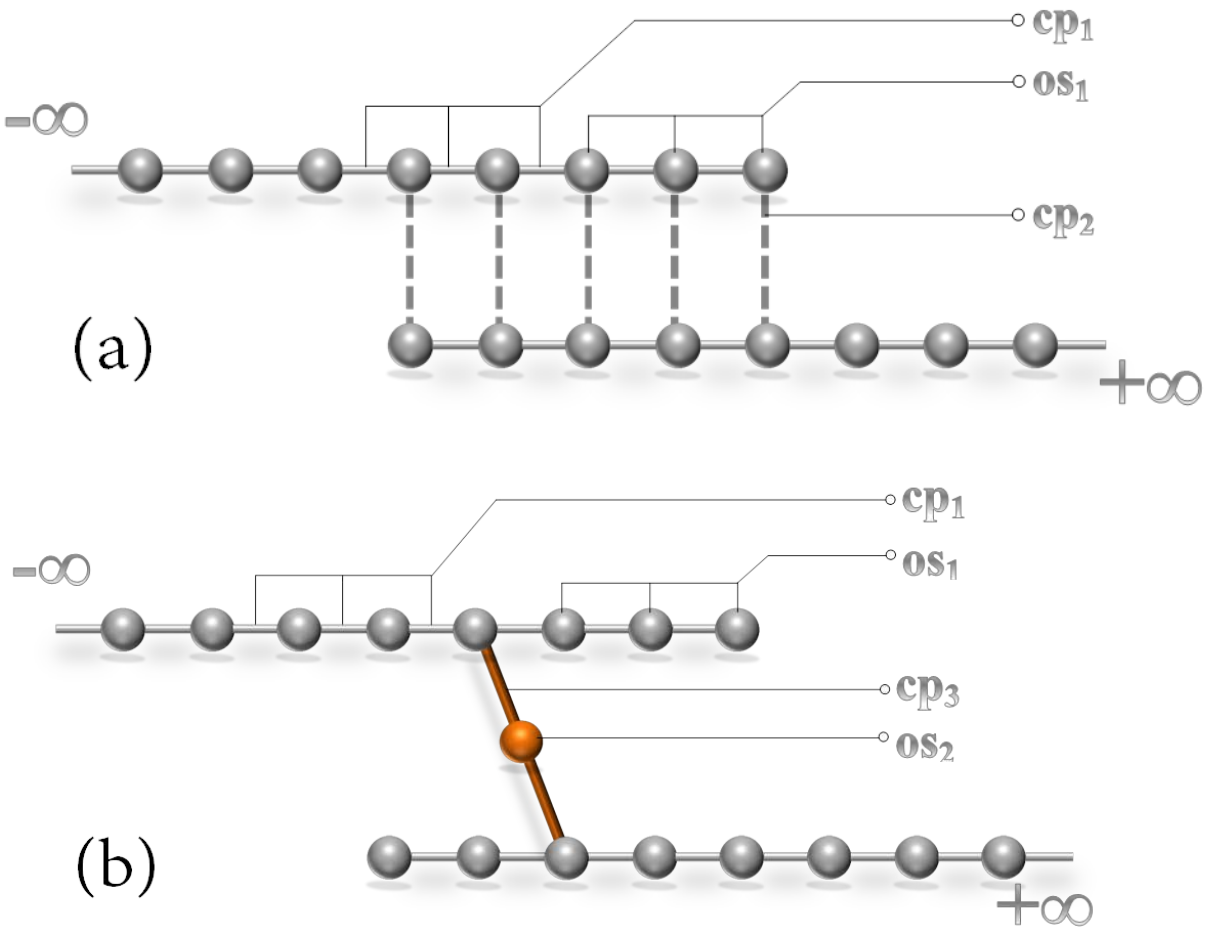

Figure 6: Tight binding toy model for graphene-silane-graphene junction. In both a and b figures, graphene monolayer is represented by one dimension chain, which consists of one-orbital per each site with onsite energy parameter os_1, graphically represented by grey balls. These orbitals, balls, connected to each other by hopping parameter cp_1. Figure (a) illustrates two semi-infinite two chains coupled to each other by weak hopping element cp_2, dashed line through five overlapped sites. Figure (b) shows the same semi-infinite chains but connected to each other through intercalated site, orange ball, with onsite energy os_2, which represents the silane molecule. The couplings between silane and the chains is represented by cp_3 as a coupling parameter. In (b), the tilted site simulates the actual molecule tilting, as it can be seen in Figure 4, and breaks the symmetry as well. The parameters cp_1, cp_2, cp_3, os_1, and os_2 are respectively equal to -0.5, -0.1, -0.5, 0, and 0.

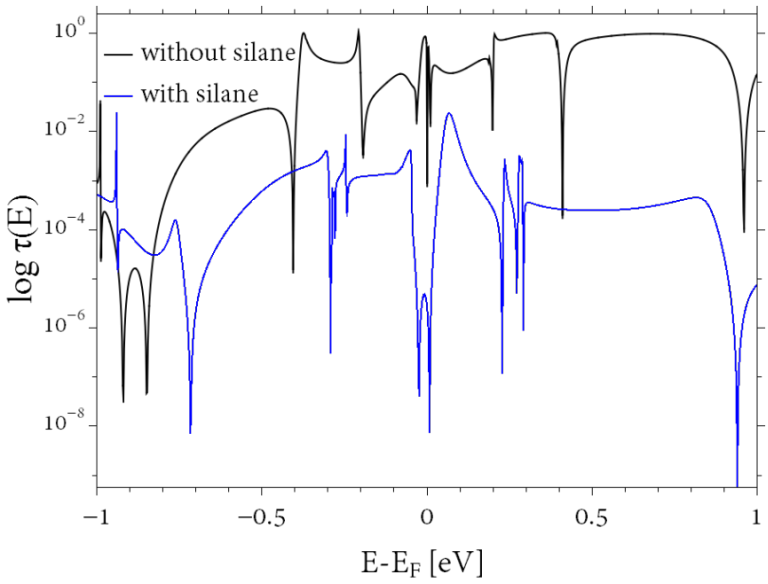

Figure 7: Using DFT , the electronic transmission coefficient curve versus energy of graphene-silane-graphene junction, where the black line represents the cross plane transmission between graphene sheets without including silane molecule, while the blue curve is for the junction with silane molecule.

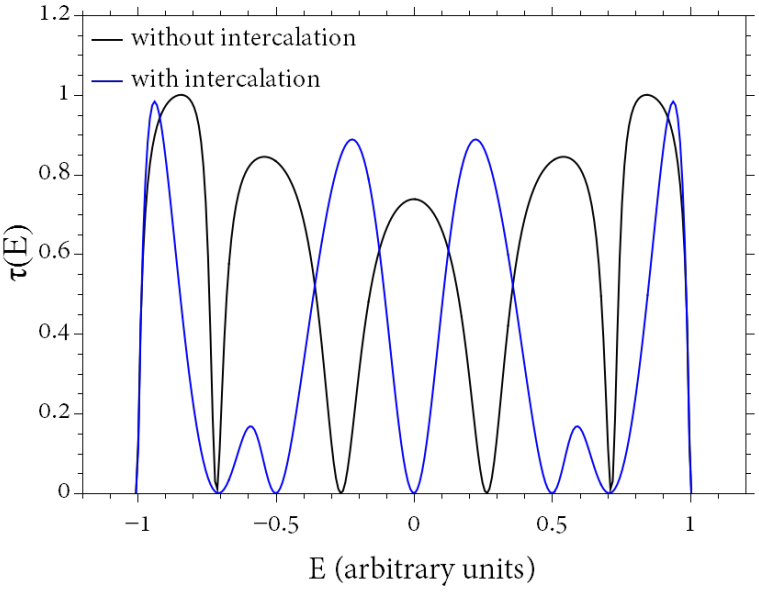

Figure 8: Energy dependence of the transmission coefficient of tight binding toy model for graphene-molecule-graphene junction.

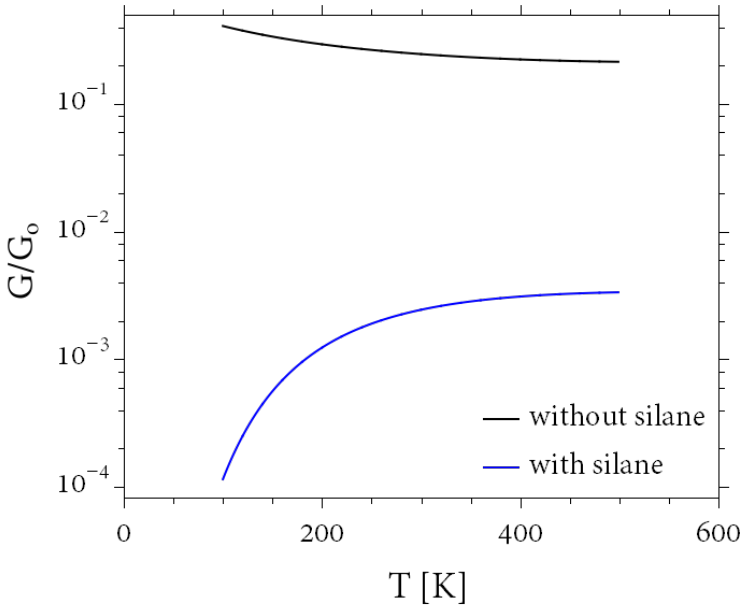

Figure 9: Using DFT, the electrical conductance as a function of the temperature. The black curve represents the junction without silane, whereas the effect of silane between the sheets is considered in the blue curve.

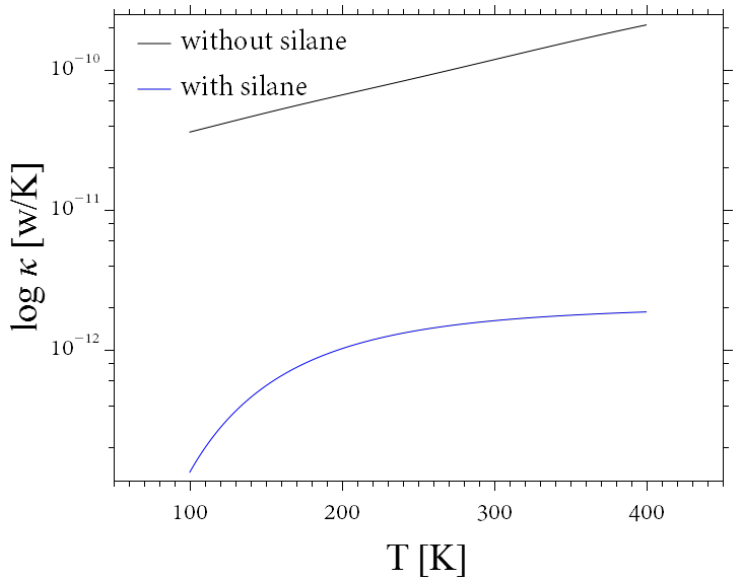

Figure 10: Using DFT, the electrical thermal conductance of the junction as a function of temperature. The black curve is the junction without silane, while the blue one is the junction with silane molecule.

The cross-plane electrical conductance has decreased due to silane, as shown in Figure 9. The conductance is the average of the transmission over a voltage or temperature range[85], i.e, it is the susceptibility of the system to the variation of the voltage or temperature[73]. Therefore, the conductance lowering is attributed to the transmission behaviour. The same argument can be used with electronic thermal conductance, Figure 10, via Wiedmann-Frantz law,

$$\frac{\kappa_e}{G} = TL, \tag{3.10}$$

where L is Lorentz number ($=\frac{\pi^2 k_B^2}{3e^2}$)[86, 87]. Furthermore, when the temperature is low, the mean free path of the electrons (l_e) is independent of temperature, and thus κ_e linearly changes with temperature. However, when temperature increases, l_e inversely relates to T, which makes κ_e temperature independent[88]. κ_e independence of T is attributed to the proportional of l_e, the distance the electron passes before being scattered[89], with the number of phonons. Therefore, when the temperature passes the Debye temperature, the number of phonons grows with temperature, and l_e decreases ($l_e \propto 1/T$). Thus, at high temperature, the phonons dominate, and the thermal conductance due to phonons dominates, the electronic contribution to the total thermal conductance will be limited [88, 90].

To discuss Peltier and Seebeck coefficients, I need to return to Eq.(3.1). In the linear response theory, one can write Eq.(3.1) as

$$\begin{pmatrix} I_e \\ I_q \end{pmatrix} = \begin{pmatrix} G & L \\ M & K \end{pmatrix} \begin{pmatrix} \Delta V \\ \Delta T \end{pmatrix}, \tag{3.11}$$

where *K, L,* and *M* are thermoelectric coefficients. In the absence of any time reversal symmetry breaking factor[1], and using the Onsager relation, which interconnects the linear response coefficients to each other [91-93], *M* can be written in terms of *L* as

$$M = -LT \tag{3.12}$$

Equations (3.11) and (3.1) lead to the following result

$$\begin{pmatrix} \frac{1}{G} & -\frac{L}{G} \\ \frac{M}{G} & K - \frac{LM}{G} \end{pmatrix} = \begin{pmatrix} R & S \\ \Pi & \kappa_e \end{pmatrix} \tag{3.13}$$

Therefore[74],

$$S \equiv \left. d_T V \right|_{I_e=0} = -\frac{L}{G} \tag{3.14}$$

$$\Pi = \left. d_{I_e} I_q \right|_{\Delta T=0} = \frac{M}{G} = ST \tag{3.15}$$

$$\kappa_e = \left. -d_T I_q \right|_{I_e=0} = -\left(K + S^2 GTK\right) \tag{3.16}$$

As a result of (3.14) and (3.15), the lower electrical conductance, the higher *S* and Π regardless of the sign, as shown in Figure 11 and Figure 12 respectively. This means that the junction permits for less heat current to cross and electrons will feel high bias on both sides. But decreasing κ_e and *G* will result in decreasing of *ZT*. However, silane has improved *ZT*, as shown in Figure 13. This anomalous behaviour of *ZT* can be attributed to the fact that the increament in *S* has overcome the suppression in both κ_e and *G*. In order to improve the figure of merit of an electronic device, scientists try either to restrain the thermal conductance, the denominator of (3.7), or enhancing the thermopower, the numerator of (3.7). With silane molecule, the latter scenario has occurred.

[1] These factors include as an example magnetic field, see the introduction of Ref..91. Jacquod, P., et al., *Onsager relations in coupled electric, thermoelectric, and spin transport: The tenfold way.* Physical Review B, 2012. **86**(15): p. 155118.

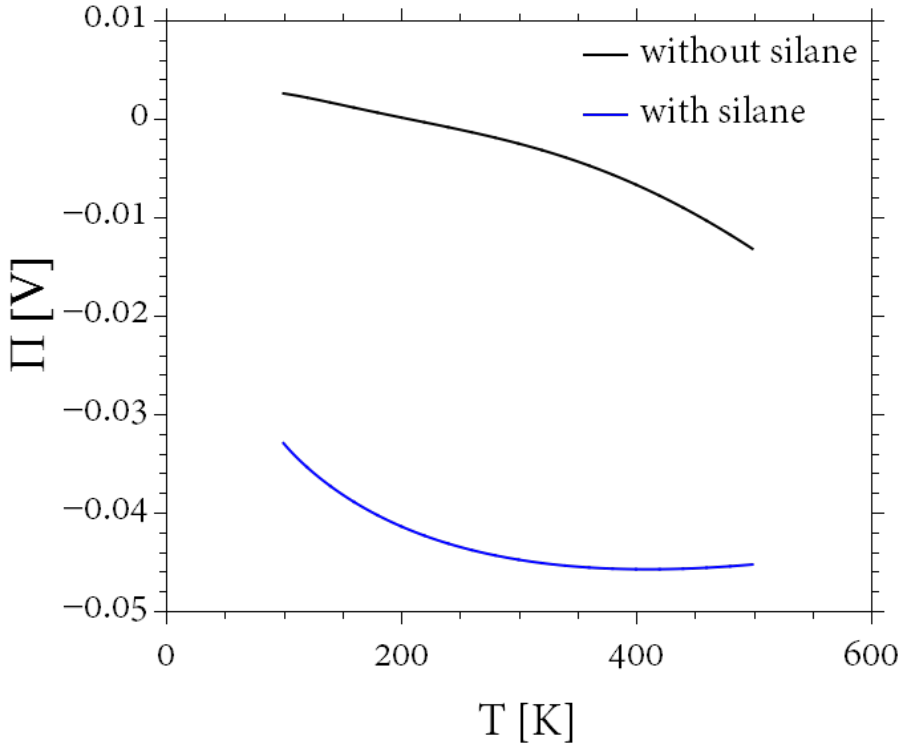

Figure 11: Using DFT, the variation of Peltier coefficient with temperature for the junction without silane, black curve, and with silane, blue curve.

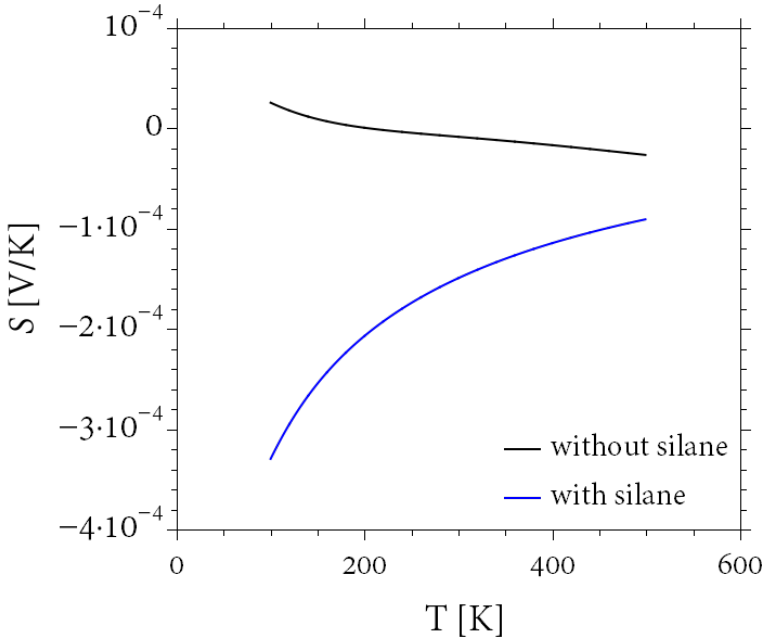

Figure 12: Thermopower change as a function of the junction temperature, where the black and the blue curves represent the junction with and without the functionalization molecule, silane

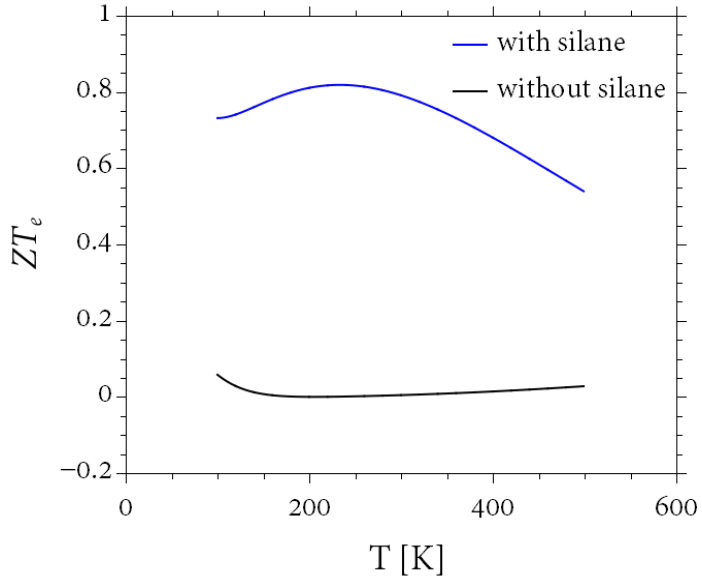

Figure 13: Figure of merit due to electrons as a function of temperature. The effect of the existence and absence of silane was considered in the blue and black curves respectively.

3.4. Synopsis

The high thermal conductivity of graphene and few-layer graphene undergoes severe degradations through contact with the substrate. Here I have shown that the thermal management of a micro heater is substantially improved by introducing alternative heat-escaping channels into a graphene-based film functionalized with amino-silane molecules. The current chapter illustrates the effect of amino-silane molecule on electronic contribution to the thermoelectric properties of graphene-molecule-graphene junction. Indeed, silane has largely affected the properties of the junction by decreasing transmission coefficient, and thermal conductance, whereas it has noticeably enhanced Peltier coefficient, and Seebeck coefficient. Furthermore, the main result of the current work is that silane has increased the figure of merit, as shown in Figure 13, of the junction which confirms its validity for electronic devices.

The main message of this project is that silane functionalized graphene can be effectively used to mediate heat in the electronic chip. Experimentally, it was monitored that the hotspot temperature was lowered by ~28 ^{o}C for a chip operating at 1,300 Wcm^{-2}. Moreover, thermal resistance measurements demonstrated an improved thermal coupling due to functionalization of the graphene.

Chapter 4 - Interplay between electronic and nano-mechanical properties of quasi-free standing graphene on SiC

4.1. Introduction

The unique electronic and mechanical properties of graphene make it attractive for the use in the nanoelectronics industry[34]. In particular, epitaxial graphene on SiC has shown great potential for integration in large-scale production due to its compatibility with complementary metal-oxide semiconductor (CMOS) fabrication process and the no need for graphene transfer (due to the insulating nature of the substrate). Due to the two-dimensional nature of graphene, the substrate will have a substantial influence on both the electronic and mechanical properties of epitaxial graphene. Thus, the vision of integrating graphene into nanoelectronic devices such as high-speed transistors[94], ring oscillators[95], integrated circuits[96] and many more depends on our ability to minimize the electronic interactions between graphene and the substrate and at the same time maintaining the high mechanical durability of graphene, resting on the SiC substrate.

Despite the reproducible control of the growth process and the excellent quality of the graphene produced epitaxial on the Si(0001) face of the 4H-SiC, the intrinsic electronic properties of graphene, such as mobility, suffer due to impurities and phonon scattering[97, 98]. Furthermore, the as-grown graphene, a partially attached graphene sheet to the substrate through covalent bonding [99], exhibits strong electron doping. The reason for the modification of both properties is the formation of the interfacial layer (IFL, also known as a buffer layer), which is a carbon layer covalently bonded to the SiC substrate [97, 100-102].

A proposed method for decoupling of the epitaxial graphene from the SiC substrate is hydrogen intercalation, which already has resulted in improved intrinsic cut-off frequency graphene field-effect transistors[103]. By annealing the as-grown graphene at high

temperatures 700-1100 °C in hydrogen environment, hydrogen penetrates underneath the graphene layers and breaks the C-Si bonds between the IFL and substrate and creates Si-H bonds. This process results in decoupling of the IFL and its transformation into a quasi-free standing graphene (QFSG), resulting in superior carrier mobility as well as reversing the carrier type from electrons to holes [97, 100-102].

Currently QFSG is the only production method that has the potential to bridge the gap between scalable and high mobility graphene, while maintaining the desirable mechanical properties and support by the substrate. Although hydrogen intercalation was systematically studied to understand the changes in the electronic and structural properties on both global[101] and local scale[104], there are currently no studies investigating the changes in the mechanical properties (i.e. stiffness) of the QFSG, which will play a crucial role in the mechanical and electronic integrity of future devices. In this work, I directly correlate the changes in the local (work function) and global (carrier mobility and concentration) electronic and local nano-mechanical (stiffness) properties upon hydrogen intercalation. For this investigation I analyse frequency-modulated Kelvin probe force microscopy (FM-KPFM) to construct a work function map of graphene samples, which provides information on the graphene layer distribution with nanometer resolution, outlining areas of different carrier concentration (i.e. thicker graphene). Moreover, transport measurements in the van der Pauw geometry provide information about the carrier concentration and mobility on global scale, without the need for patterning devices. In particular, the method demonstrates the change of the carrier type, i.e. from n- to p-type, and significant 4-fold enhancement in mobility following the intercalation process. The correlation with the nano-mechanical properties is performed using ultrasonic force microscopy (UFM), which maps the stiffness of the material with nanometer resolution, exposing the changes that the graphene samples undergo following decoupling from the SiC substrate. These structural properties were also obtained from density functional theory (DFT) code SIESTA by taking the difference between the potential at the surface layer (graphene) and the potential in the vacuum. In addition, in order to calculate the stiffness, I first calculated the total energy for different separations

between the SiC and graphene, and then differentiated the total energy with respect to these distances.

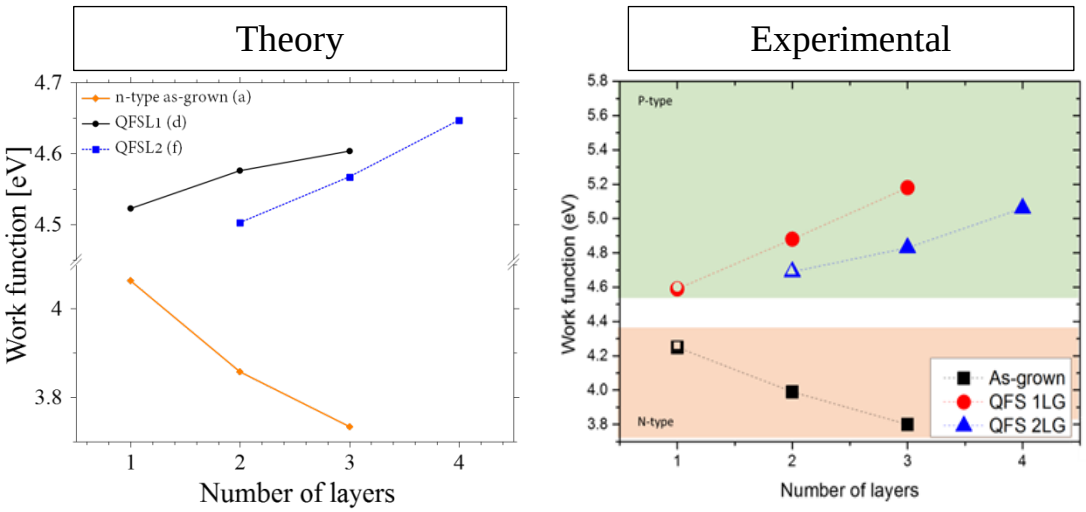

Figure 14; A comparison between theortical calculations (left) and experimental measurements (right). The results show good agreement

For this investigation I consider three types of samples, namely: i) as-grown one layer graphene (1LG); ii) quasi-free standing one layer graphene (QFS 1LG) obtained as a result of hydrogen intercalation of IFL; iii) quasi-free standing two layer graphene (QFS 2LG) obtained as a result of hydrogen intercalation of 1LG. A comparison between experimental measurements and my theoretical calculations are shown in Figure 14, wich reflects a good agreement. UFM measurements demonstrate that following hydrogen intercalation the graphene stiffness decreases, i.e. from 860 N m-1 (as-grown) to 454 N m-1 for the QFS 1LG. Comparison of our results with the previous studies demonstrates that the QFS 1LG still exhibits higher stiffness than the suspended exfoliated graphene (340 N m-1)[105], while retaining the mechanical integrity and high mobility making is suitable for high speed electronics (3900 cm2 (V•s)-1). This is not the case for the QFS

2LG, where the measured stiffness is 211 N m-1, lower than the exfoliated graphene measured by Lee et. al.[105], and at the same time exhibits lower mobility compared to the QFS 1LG. Furthermore, pockets of mobile trapped excess hydrogen have been observed near the edges of the QFS 2LG, a situation which should be avoided when fabricating nano-electronic devices. It is therefore essential that future graphene-based high speed nano-electronics utilize the superior quality, carrier mobility and stiffness of the QFS 1LG.

4.2. Methods

4.2.1. Optimization

The optimization is performed using the supercell approximation [67] which is explicitly introduced by Junquera *et al.* [106] in SIESTA. The reason for this approximation is to retain the periodicity of the plane wave basis in space [107], namely 3D for bulk, 2D for surface, and 1D for chains. Therefore, and as result of the 2D surface of SiC/graphene interface, the current supercell is kept periodic in *xy*-plane in order to cancel out any dipole potentials which result from charge accumulation at the edges[106] and is discontinuous in *z* direction by imposing 15 A^o vacuum region. The SiC/graphene supercell is composed of a commensurate number of carbon atoms for monolayer graphene on one side and the silicon carbide on the other side. To consider the effect of the intercalation of hydrogen between SiC and graphene, I have varied the concentration of the hydrogen from 0% to ~200%. The introduced hydrogens have only a direct interaction with the last Si layer and the first graphene sheet. Thus the hydrogen concentration ($H_{concentration}$) is calculated as the percentage required to saturate all Si atoms at the surface of the SiC,

$$H_{concentration} = \frac{H_{atom}}{Si_{atom}} \times 100\%, \qquad (1.1)$$

where H_{atom} and Si_{atom} represent the number of hydrogen and silicon atoms respectively.

The relaxed geometries of the cell were calculated through the aforementioned Quantum Chemistry code, SIESTA [12]. First, I overcome the k-point error by converging the total energy with Brillion zone of 4×4×1 k points and a plane wave basis with 300 Ry mesh cutoff radius[67]. Double zeta polarized basis sets have also been used to describe the long range interactions and charge distribution. The system is considered relaxed when the forces between atoms are less than 0.03 eV/Ang. Along the *z* direction, I implemented the dipole correction[108] to cancel out the dipole gradient surrounding the surface. Moreover, an extra charge has been imposed to the system to simulate the doner or/and acceptor graphene. All the above characteristics have been implemented within the Van der Waals approximation of the exchange-correlation via the BH approach[109, 110]. the Van der Waals (vdW) functional takes into account delocalized long-range interactions[110, 111], and has proved to be successful for a number of system such as the multilayer ones and system with physisorption interactions[112].

The relaxed structures are shown in Figure 15. In order to have a systematic study, I have simulated five structures with 0%, ~33%, ~60%, 100%, and ~200% hydrogen concentrations, which are represented by Figure 15a, b, c, d, and e respectively. The last unit cell is a model for a quasi free standing layer of graphene type two (according to the experimental nomeclature). Furthermore, for each concentration the number of graphene layers has been increased from one layer until 3 layers, samples can be seen in Figure 16.

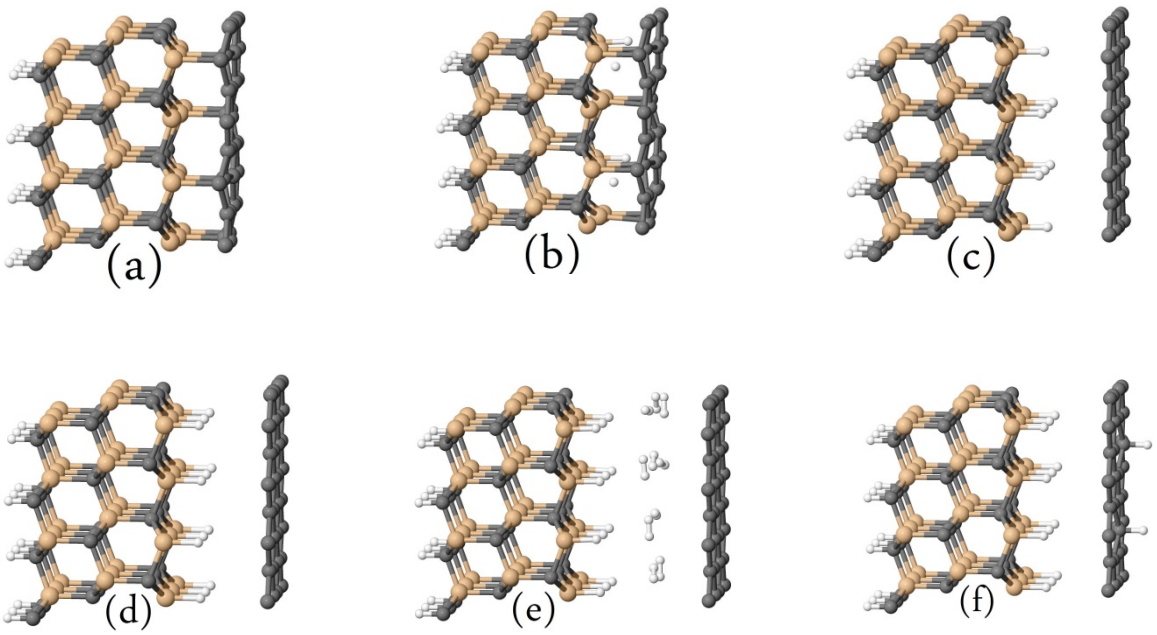

Figure 15: Unit cells for interfacial graphene layer (IFL) on top of SiC substrate with a) bare SiC and b) 30% passivated with H. Quasi free standing graphene layer on top of SiC substrate with c) 60% passivated with H, d) 100% passivated with H, and e) 100% passivated and covered with H_2 molecules. f) shows a SiC substrate and the QFSL graphene are respectively passivate with 100% and 6.25% with H. The percentage is defined as 100×(the total number of hydrogen atoms) / (the total number of atoms of the attached surface).

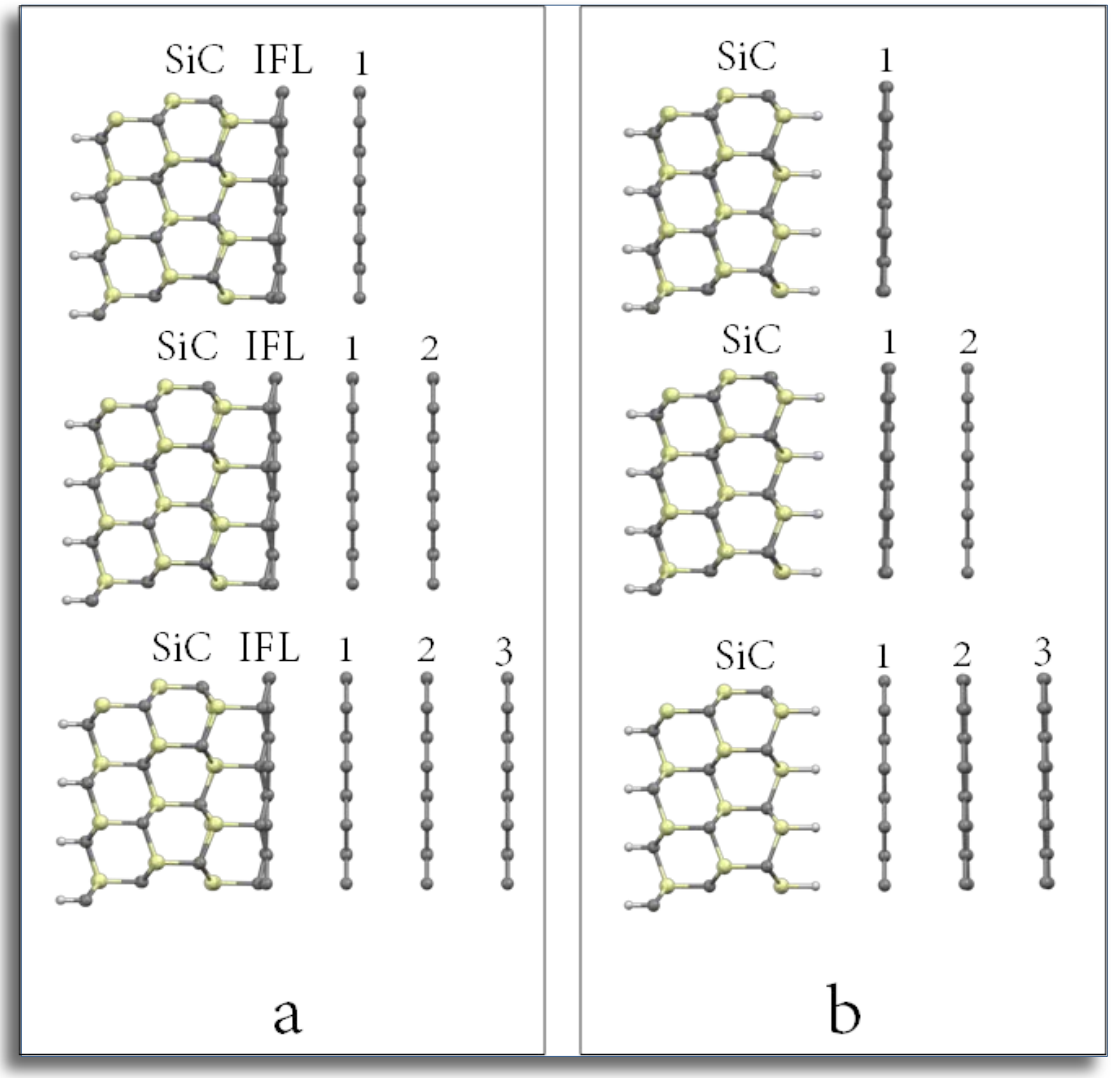

Figure 16: Increasing the number of graphene layers on top of two SiC unit cell samples. In total, three graphene monolayers are attached to the surface of SiC one layer at a time. The graphene layers are represented by the numbers from one to three and the IFL is the acronym of the graphene interfacial layer. Unit cell (a) consists of SiC substrate interacts directly to a graphene interfacial layer (IFL) with no intercalated hydrogen atoms at the interface. Whereas, the concentration of hydrogen is 100% in unit cell (b) and then the fully saturated SiC substrate is attached to the graphene layer, one layer per step.

4.2.2. Workfunction

After structure optimization, I calculated the work function as the energy required to extract an electron from the surface of the system [113]. The work function simulation was conducted for the surface layer with six hydrogen concentrations (0%, 8%, 17%, 25%, 33%, and 100%), where 0%, 33%, and 100% concentrations stand for (a), (b) and (d) unit cells in Figure 15. In addition, I have also calculated the variation of the work function with number of graphene layers for as-grown, quasi-free standing graphene type-1 (QFSL1) and quasi-free standing graphene type-2 (QFSL2), illustrated in Figure 29. The profile of the potentials of the slabs can be obtained by means of the Macroave, SIESTA post processing code for charges and potentials[12]. Macroave takes the planar average along the *z* direction for the *xy*-plane potentials and charges. As a result, one can infer the vacuum energy level (E_{vac}), which is required to calculate the work function (W) as [114, 115]

$$W = E_{vac} - E_F, \tag{1.2}$$

where E_F is the Fermi level. Now, equation (4.2) is not as a simple as it looks. The reason for that is the E_{vac} term. Therefore, to clearify the meaning E_{vac}, I shall outline the SIESTA definition for the potentials used to produce the potential at vacuum.

SIESTA defines the total Hartree potential ($\xi_T^H(\vec{r})$) in real space as [116]

$$\begin{aligned} \xi_T^H(\vec{r}) &= \xi_{ion}^{local}(\vec{r}) + \xi_{elec}^H(\vec{r}) \\ &= \sum_J \xi_J^{local}(\vec{r}) + \xi_{elec}^H(\vec{r}), \end{aligned} \tag{1.3}$$

where the total Hartree potential consists of two part:

1. The ionic contribution $\xi_{ion}^{local}(\vec{r})$ $\left(=\sum_J \xi_J^{local}(\vec{r})\right)$ is the long range contribution to the Hartree potential. Where $\xi_J^{local}(\vec{r})$ represents the local part of the pseudopotential and *J* refers to the atomic site.
2. The electronic contribution $\xi_{elec}^H(\vec{r})$ emerges from the charge density $\left(n^{elec}(\vec{r})\right)$ of the electrons, which can be defined as

$$\begin{aligned} n^{elec}(\vec{r}) &= n^{atom}(\vec{r}) + \delta n(\vec{r}) \\ &= \sum_J n_J^{atom}(\vec{r}) + \delta n(\vec{r}), \end{aligned} \tag{1.4}$$

The corresponding potentials for each term in the last equation are [116]

$$\xi_{elec}^{H}(\vec{r}) = \sum_J \xi_J^{atom}(\vec{r}) + \delta\xi(\vec{r}), \tag{1.5}$$

where

- $n^{atom}(\vec{r})$ $\left(=\sum_J n_J^{atom}(\vec{r})\right)$ is the sum of the intact atomic valence charge densities[114].
- $\delta n(\vec{r})$ is the deformed charge density stems from atomic interactions

By substituting (4.5) in (4.3), one obtains

$$\begin{aligned} \xi_T^H(\vec{r}) &= \sum_J \xi_J^{local}(\vec{r}) + \sum_J \xi_J^{atom}(\vec{r}) + \delta\xi(\vec{r}) \\ &= \sum_J \left[\xi_J^{local}(\vec{r}) + \xi_J^{atom}(\vec{r})\right] + \delta\xi(\vec{r}) \\ &= \xi^{neut}(\vec{r}) + \delta\xi(\vec{r}), \end{aligned} \tag{1.6}$$

where

$$\xi^{neut}(\vec{r}) \equiv \sum_J \left[\xi_J^{local}(\vec{r}) + \xi_J^{atom}(\vec{r})\right], \tag{1.7}$$

represents the neutral atom potential. The three potential contributions to the total Hartree potential can be schematically shown in Figure 17. By taking the average of the total Hartree potential[116]

$$\left\langle \xi_T^H(\vec{r}) \right\rangle = \left\langle \xi^{neut}(\vec{r}) \right\rangle + \left\langle \delta\xi(\vec{r}) \right\rangle \tag{1.8}$$

Thus [117, 118],

$$E_{vac} = \left\langle \xi_T^H(\vec{r}) \right\rangle_{slab} - \left\langle \xi_T^H(\vec{r}) \right\rangle_{vac} \tag{1.9}$$

Using the definition of Eq.(4.9), one can calculate the work function.

4.2.3. Stiffness

In order to calculate the stiffness (X) due to the interaction between the mono/multilayer/IFL graphene and the substrate, one needs to find the gradient of the total energy with distance. Since the stiffness is the resistance of the system to the applied displacement[119], it is defined

$$X = \frac{dF_{\perp}}{dh}, \tag{1.10}$$

where h is the separation distance between two adjacent layers, and $F_{\perp}$ is the vertical force [120], which is defined as

$$F_{\perp} = -\frac{\partial E}{\partial h} \tag{1.11}$$

Therefore, Eq.(4.10) can be rewritten as

$$X = -\frac{\partial^2 E}{\partial h^2} \tag{1.12}$$

In the measurements, the cantilever of an ultrasonic force microscopy is used to push the surface of the system by applying two different forces and recording the corresponding distance variations. Experimentally, the stiffness is measured via

$$X_{\exp} = \frac{dF}{ds}, \tag{1.13}$$

where s is the distance between two layers. Therefore, the total energy has been calculated in steps, where each step means a change in the distance between the SiC and the attached layer. During the simulation, the SiC substrate was fixed and let the next bound layer allowed to move. Next, the resultant total energy curve was fitted to a parabola, which can be seen in Figure 18.

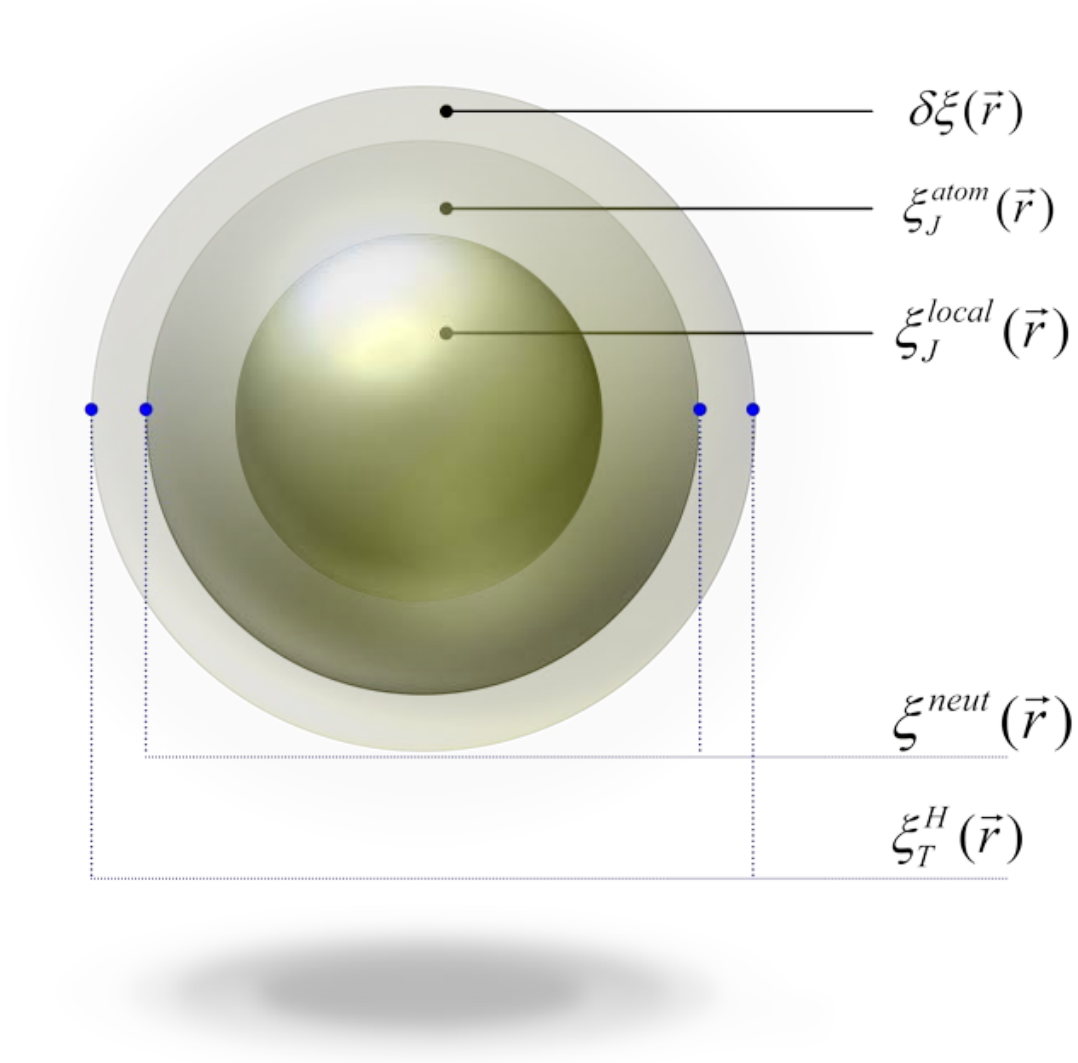

Figure 17: A schematic representation of the atomic potentials. The $\xi_J^{atom}(\vec{r})$ term represents the local ionic part of the atomic potential, $\xi_J^{atom}(\vec{r})$ is the valence charge density potential, $\delta\xi(\vec{r})$ is bonding charge density potential, the superposition of the first two potentials is represented by $\xi^{neut}(\vec{r})$, and finally $\xi_T^H(\vec{r})$ results from the sum

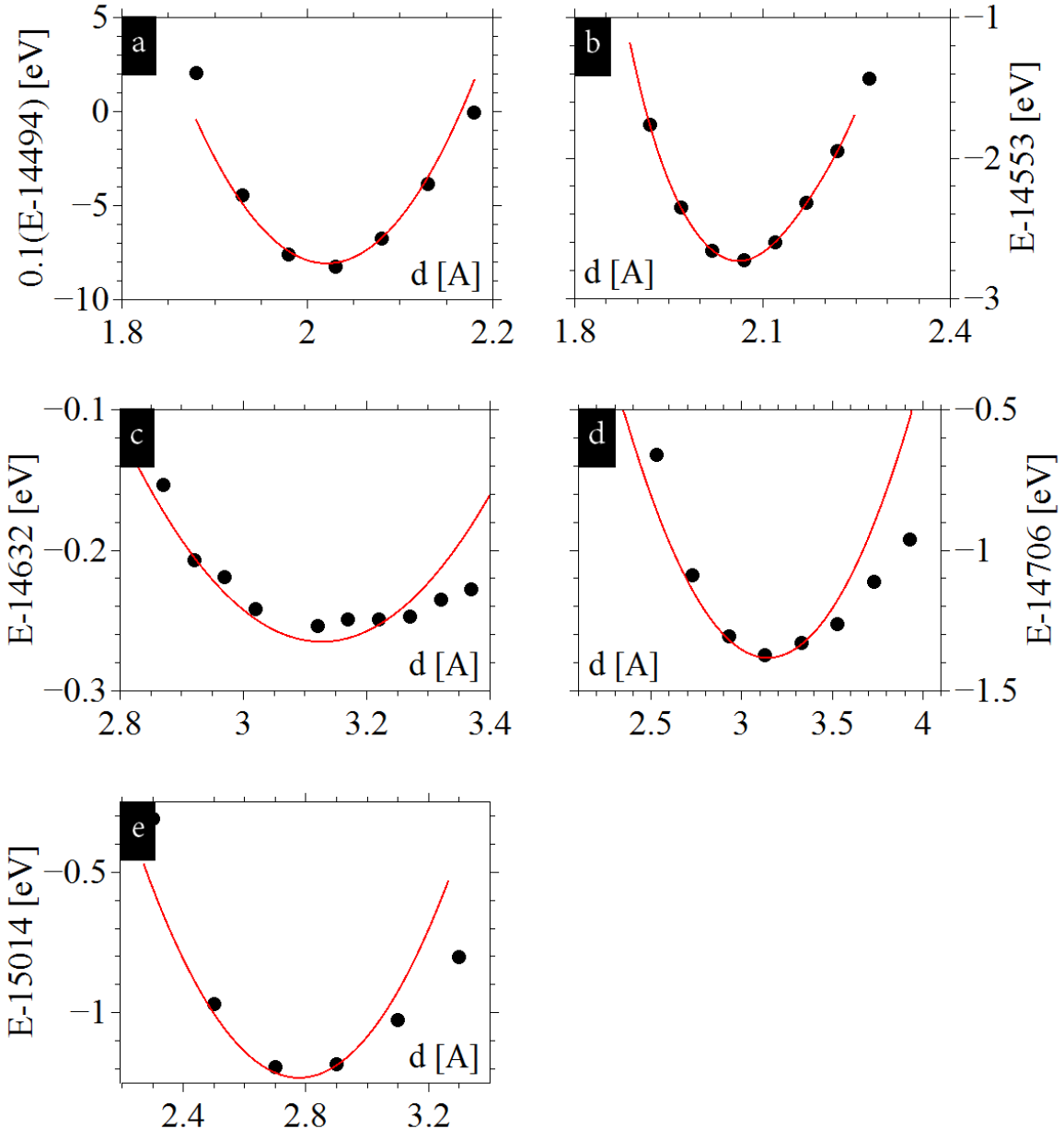

Figure 18: Stiffness fitted curves for the first five unit cells shown in Figure 14, where labels a-e correspond to the same labelling used there. In all figures, the solid black circles represent DFT calculations and the red lines stand for the fitted curves.

4.3. Results and discussion

The calculations were set up to study the effect of two variables: hydrogen concentration and the number of graphene layers. Therefore, the current section has been arranged to discuss the work function and stiffness corresponding to each one of these variables. As a result, I will divide my discussion into two sub-sections, one for each variable.

4.3.1. Hydrogen Concentration

The main features are illustrated in Figure 19 and Figure 24 which show the variation of stiffness and work function with hydrogen concentration respectively. The letters from (a-e) refer to the unit cells shown in Figure 15.

The stiffness calculations show that unit cells (a) and (b) have the highest values with a very sharp variation compared to the last three unit cells. One should remember that the unit cells (c-e) have a high concentration of hydrogen atoms intercalating the interface between the surface silicon layer and the first graphene monolayer. As a result of the increasing of the penetrating hydrogen atoms, the separation distance between the interfacial layers increases, as shown in Figure 20. Furthermore, moving SiC and graphene apart from each other will lessen the direct interaction[121], as shown in Figure 22 and Figure 23, and thus the binding energy between them will drop with the number of hydrogen atoms. In order to get a deep analysis, I have plotted the partial density of states for each element in three unit cells, where the SiC has been 0% (a), 33% (b), and 100% (d) saturated with hydrogen. The energy levels are shifted so that the Fermi energy (E_F) is located at 0.0 eV.

With no hydrogen intercalating between the surface silicon and graphene layer, Figure 22a shows that there is a strong interaction between graphene and silicon at the Fermi with a localized state, indicating the presence of the covalent bonding. This localized peak can be attributed to the dangling bonds of Si atoms[121] at the interface, which can be verified by the local density of states, as illustrated in Figure 23a. This is also

supported by the dominating weight of silicon over carbon atoms, which previously showed by Figure 22a. Furthermore, there is then an energy gap of approximately 1.5 eV to the left of the Fermi in consistent with other experimental[122] and theoretical results[121, 123]. This huge deviation from normal graphene behaviour is due to the strong coupling between the first graphene layer, so-called interfacial layer, and the Si terminated substrate[123].

At 33% saturation with hydrogen for the surface-silicon layer, Figure 22b, the Fermi level sits in middle of the gap of approximately 1 eV width, which is less than the gap of the first case by nearly 30%. Moreover, a highly bound state is present near the HOMO level at approximately -0.75 eV from the Fermi. All these results have appeared as the distance between the interacted layers elongated due to the extra hydrogen atom. Indeed, DFT calculations show that the averaged distance between graphene and SiC substrate has changed from 2.314 A to 2.482 A for the cases of 0% and 33% respectively. Meanwhile, it is well known that the Si-C interactions at the interface mainly depend on the structure of the interface [124]. Therefore, the Si-C covalent bonding would fade away as the Si and C atoms detach farther from each other. A comparison between Figure 22a and Figure 22b points to the fact of such a weak interaction. Related to this, carbon nanotubes (CNT) have also shown the same behaviour as a function of the hydrogen concentration between the tube and the substrate[125], suggesting to a sort of universal behaviour for all carbon allotropes on SiC layers. For CNT, Miwa *et al.* have explained this behaviour to the strong adsorbing of the CNT to the substrate for low concentration, while a physisorption relation governs the Si-C interface at high or fully saturated surface[125].

Finally, the fully hydrogen saturated silicon/graphene interface, Figure 23d, shows a prominent domination of carbon states in the HOMO and LUMO level. Moreover the gap has disappeared and the Dirac point of the graphene has emerged. The interface separation distance has increased to become 4.6775 A, whereas both charge transfer and bonding between the silicon and carbon at the interface are negligible. The shallow states of silicon over a region of approximately 2.0 eV confirms the increasing role of the carbon atoms of the graphene sheet, which is supported by the local density of states,

shown in Figure 23d. The emergence of the Dirac point and the delocalized state over graphene sheets are both characteristics of an unperturbed graphene sheet. Therefore, one can conclude that increasing the hydrogen concentration between the substrate and the graphene will support the cleavage between them, resulting in a fully saturated and stable substrate and independent graphene monolayer. This results are in high consistent with the research data of Xu *et al.*[124].

Another result is that unit cell (b), Figure 21, shows a distinctive outcome. Indeed, the binding energy of structure (b) exceeds all other structures. This can be attributed to the full saturation of the surface silicon atoms by both the intercalating hydrogen and the graphene atoms. Comparing the partial density of states of Figure 22a and Figure 22b reveals the increasing role of the hydrogen atoms which contributes to this distinctive result. Whereas, the imperfection in the saturation between directly attached graphene to SiC is due to lattice mismatch between their unitcells. Such mismatch creates some dangling bonds at the interface, which can be compensated by a certain amount of hydrogen atoms, as it is mentioned before.

The work function, on the other hand, exhibits a trough at low levels of hydrogen, between 0% to 25%. Then a noticeable growth can be seen at 33%, which then shows a gradual increasing up to 100%. After that, a slight change can be recognized even when the number hydrogen atoms is a twice larger than the surface hydrogen atoms, where the work function approaches the value of a free graphene sheet. I should confirm here that I have different surface structures owing to the optimization, which renders the surface adapting the optimum shape. Therefore, comparsion between such structures requires a standard reference, such as the Fermi level of the system. This level, provided we use the same temperature, is the most valid refrence, since it is always located between the occupied and empty states regardless of the structure. Based on that, the Fermi level can be considered as a reflection for doping concentration [126], i.e. the hydrogen intercalating level. Figure 24b shows that the Fermi energy decreasess with the number of hydrogen atom penetrating the interface. The existence of hydrogen at the interface can be regarded as a doping, which enhance the separation distance between SiC substrate

and the graphene. As a result of this distance inverse, the work function approaches the value of a free graphene monolayer without equaling it due to charge transfer from hydrogen atom as shown in Figure 25. Therefore, one can easily peel the graphene sheet on top of SiC layer, which is the reason for calling it quasi-free standing graphene.

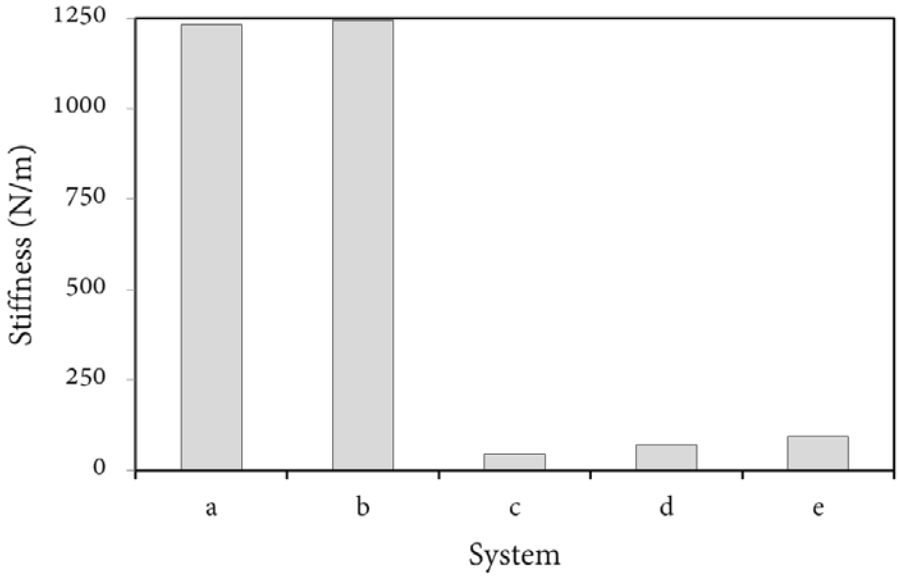

Figure 19: The stiffness for all structures a-e, illustrated in Figure 14, is presented. The stiffness is calculated by plotting the gradient of the total energy of unit cell with separation distance between SiC substrate and the first carbon layer. The considered structures are: a) bare SiC in contact with interfacial graphene and b) SiC with 30% passivated with H in contact with interfacial graphene. Whereas a QFSL graphene is on top of SiC with c) 60% passivated with H, d) 100% passivated with H, and finally e) 100% passivated hydrogen and covered with H_2 molecules.

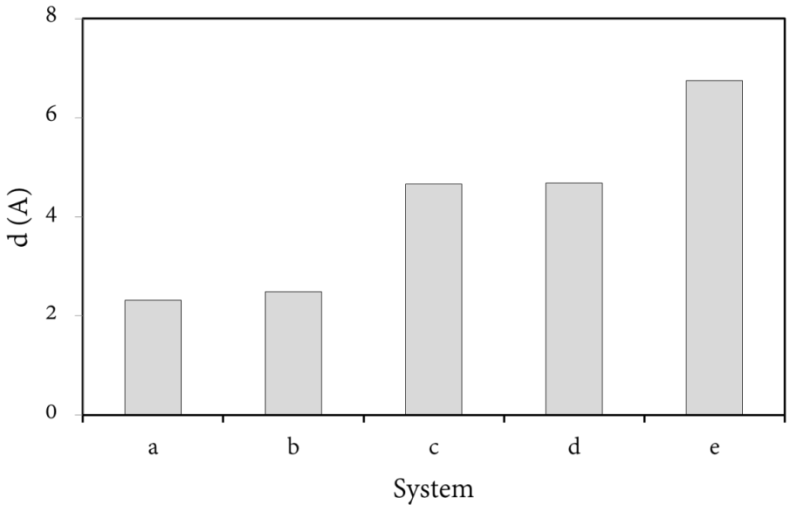

Figure 20: The minimum-energy average distance between the SiC substrate and the first layer of carbon atoms as a function of concentration of hydrogens intercalated at the interface. Where x-axis letters represent the molecules in Figure 14, which are: a) bare SiC in contact with interfacial graphene and b) SiC with 30% passivated with H in contact with interfacial graphene. Whereas a QFSL graphene is on top of SiC with c) 60% passivated with H, d) 100% passivated with H, and finally e) 100% passivated hydrogen and covered with H_2 molecules.

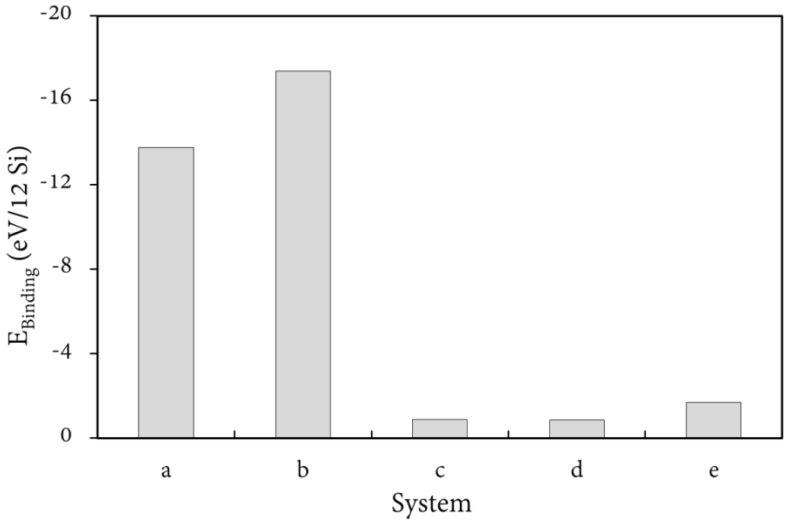

Figure 21: Binding energy between SiC and the first carbon layer for structures a-e, with different concentrations of intercalated hydrogen atoms. The percentage is calculated relative to the total number of the surface silicon atoms. The letters in the x axis are: a) bare SiC in contact with interfacial graphene and b) SiC with 30% passivated with H in contact with interfacial graphene. Whereas a QFSL graphene is on top of SiC with c) 60% passivated with H, d) 100% passivated with H, and finally e) 100% passivated hydrogen and covered with H_2 molecules.

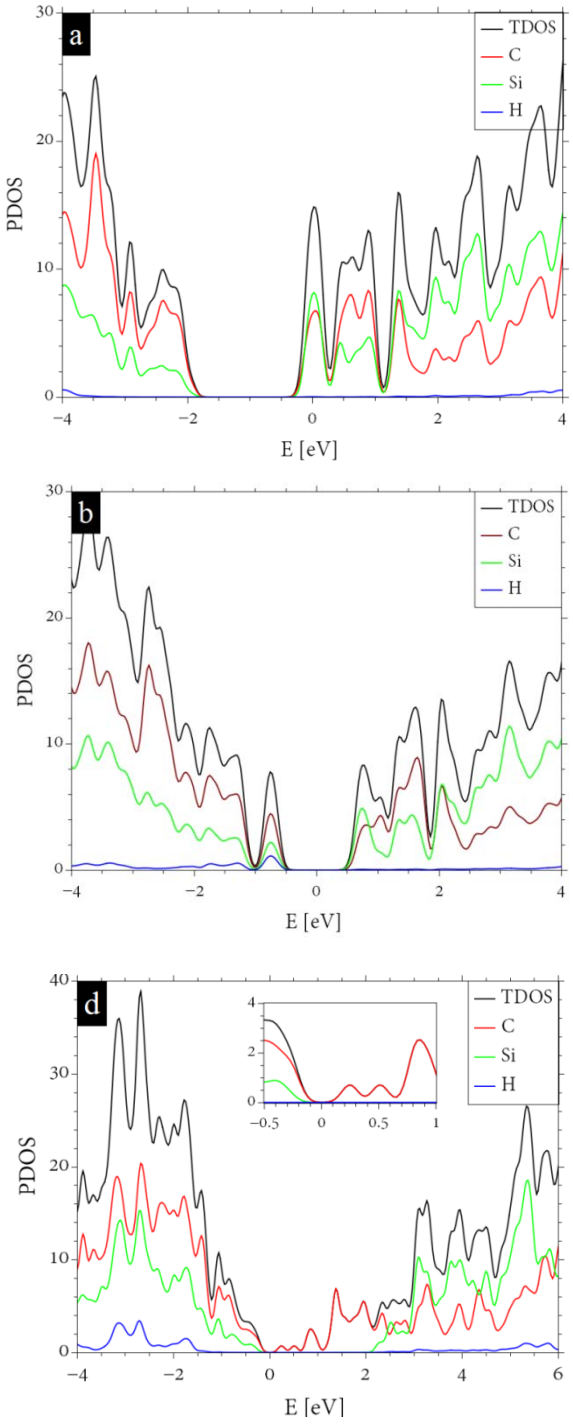

Figure 22: Partial density of states of SiC substrate covered with monolayer of graphene and saturated with (a) 0% hydrogen, (b) 33% hydrogen, and (d) 100% hydrogen. The labels were chosen so as to match the corresponding unit cells in Figure 14. Fermi level is set to be at zero for clarity in all panels. The inset in panel (d) shows the region on both sides of the Fermi energy, where levels to the right are carbon dominated which refers to a non-bonding region.

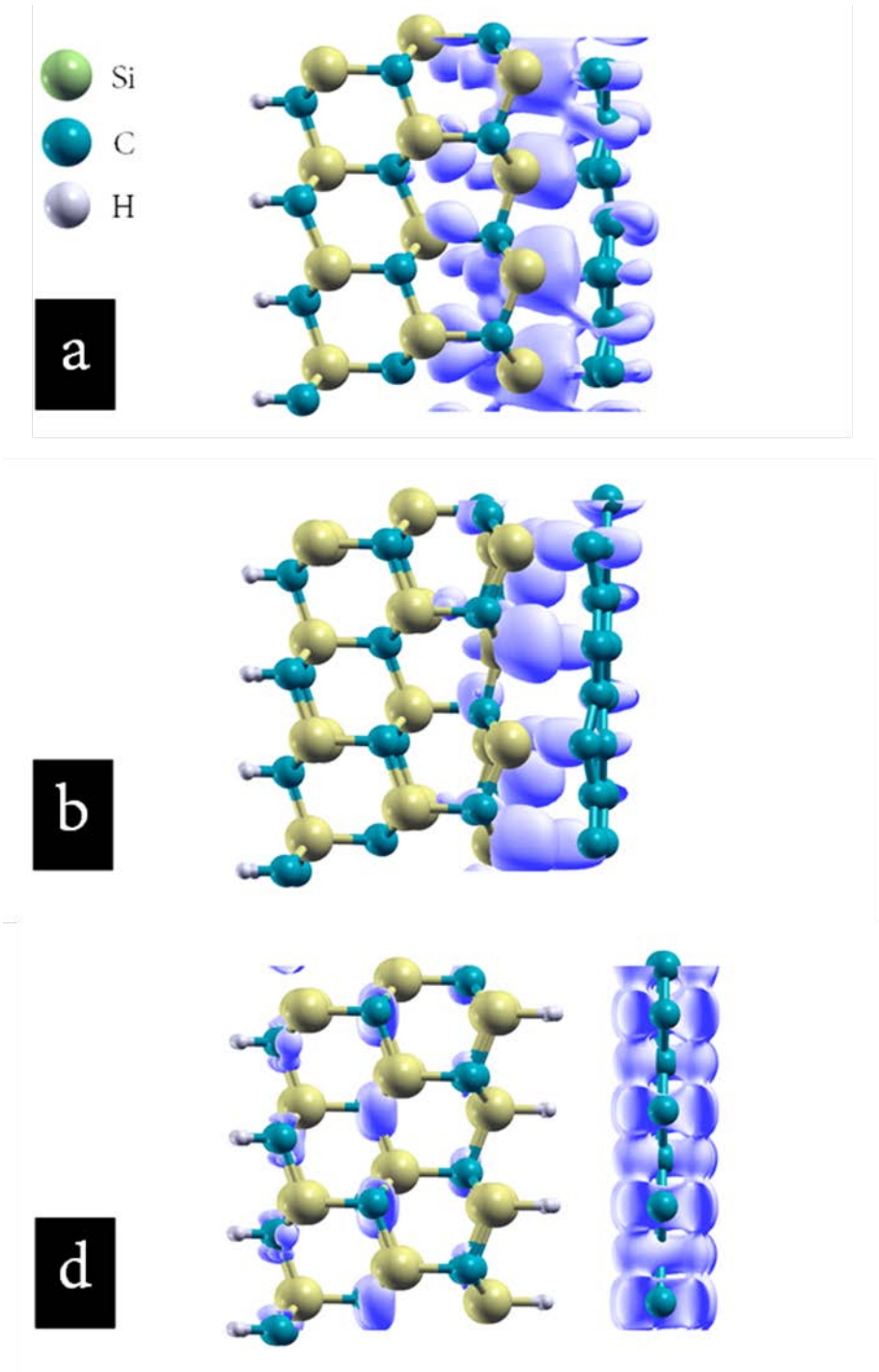

Figure 23: Local density of states (blue cloud) at Fermi energy of SiC unit cells corresponding to the PDOS illustrated in Figure 22. Labels of the panels were adapted to reflect to the related unit cells illustrated in Figure 15. Silicon, carbon, and hydrogen atoms are characterized by green, gray, and white colours respectively.

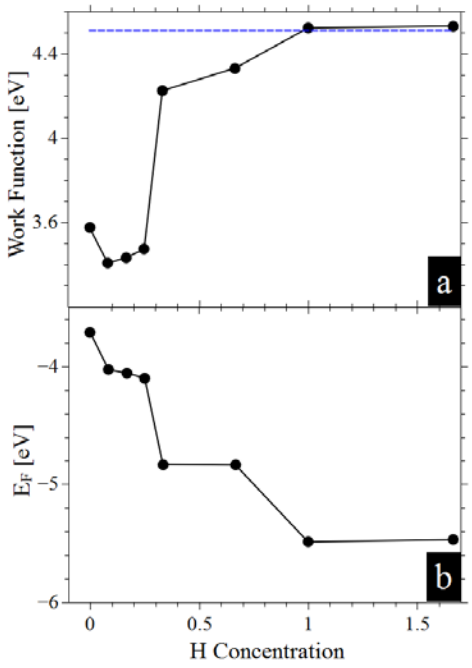

Figure 24: (a) Work function of SiC as a function of hydrogen concentration at the interface between SiC substrate and the surface carbon layer. (b) Fermi level variation with hydrogen concentration fraction, which is defined as the total number of hydrogen atoms over the total number of surface silicon atoms.

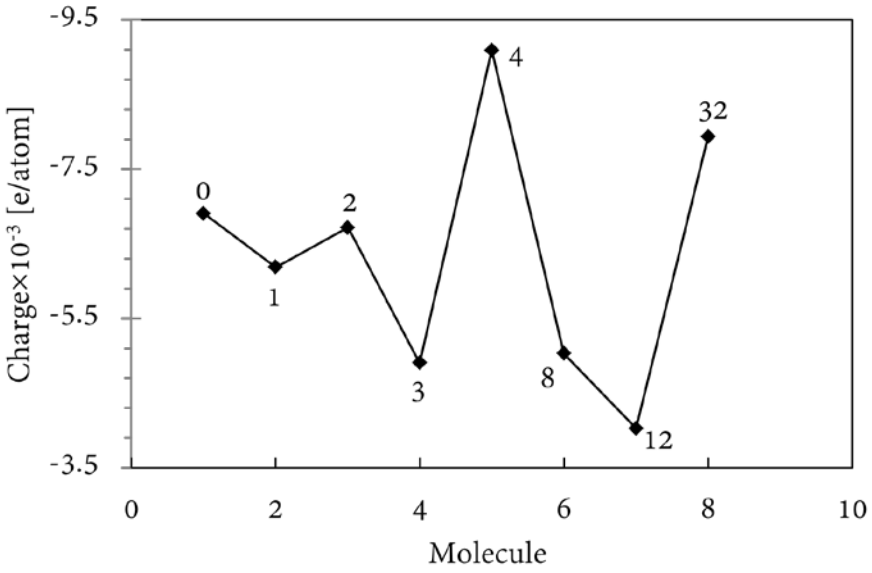

Figure 25: Extra net charge accumulated on the surface graphene layer covering the SiC unit cell for different numbers of the intercalating hydrogen atoms. These numbers range from zero hydrogen, i.e. clean Si-graphene surface, to 32 atoms. The labels next to each point refer to the corresponding number of hydrogen atoms at the interface.

4.3.2. Number of graphene layers

The first property of interest in this section is the stiffness, which shows an inverse relation with the number of graphene layers for all first five unit cells, shown in Figure 15. This decrease can be attributed to the increment in the separation distance between the interfacial/first graphene layers[121], as shown in Figure 27. Another prominent result is the variety of stiffness values with respect to the adjacent layers, illustrated in Figure 28. According to the DFT calculations, one can find that there are three values of spring constants. The first and strongest one is stiffness between the interfacial graphene layer and the surface silicon layer. Such strength results from high covalent interaction between carbon atoms in graphene and silicon atom in the substrate[127], as it can be inferred from the local density of states, seen in Figure 23a and 23b, and binding energy graph, Figure 21, which reaches its maximum value at 33% concentration of hydrogen. The second spring constant is one between any two adjacent graphene layers. This type is less than the first one and greater than the third type of spring constant. The third level is the stiffness between the surface graphene layer and the substrate in the presence of hydrogen between them. Obviously, hydrogen atoms ease the detachment between graphene and SiC due to the full saturation of SiC, on one hand, and the long distance between SiC and graphene on the other hand. Furthermore, the first/buffer graphene layer protects the higher layers from the effect of the substrate[121]. For all above mentioned reasons, Figure 26, three categories of stiffness can be recognized clearly: ~1200 N/m, ~ 70-95 N/m, and ~ 25-45 N/m.

The calculation of the above three spring constants can be summarized as follow. Figure 28 shows different values of stiffness of interest. For example γ_1 and γ_3 can be computed by fixing the spacing between the three graphene sheets and then computing the energy curvature as a function of the distance between the left-most graphene sheet and the SiC. Similarly γ_2 can be computed by fixing the spacing between the middle and right-most graphene sheets and the distance between the left-most graphene sheet and the SiC and then computing the energy curvature as a function of the distance between the left-most graphene sheet and the middle graphene sheet.

The second property is the workfunction which shows two distinctive behaviours. The first trend is shown by QFSL1 and QFSL2 where the work functions grow with the number of the layers, whereas it declines for as-grown graphene. Figure 30 and Figure 31 explain the origin of this trend. Before discussing the results I first explain the calculation method.

The electric dipole moment vector $\vec{P}(r)$ is calculated,

$$\vec{P}(r) = qd, \qquad (1.14)$$

where q is the charge difference between the directly attached graphene layer (negative) and the right most hydrogen layer (positive), and d is the separation distance between these two layers/charges. Mattausch and Pankratov [127] have shown that the interfacial region mainly controls the characteristics of the surface of the junction. One of their results has shown that charge transfer between the interfacial graphene and the substrate controls the value of the surface work function via an internal induced electric dipole moment vector. Depending on Mattausch and Pankratov findings, I have found that when the charge difference increases, the dipole increases, and thus the work function decreases as a result of the repulsion of the negative charges, as seen for as-grown. However, QFSL1 and QFSL2 show the opposite trends, where the effect of this repulsion on the outermost graphene layer is reduced as the number of layers is increased. Hence the work function increases with the number of layers.

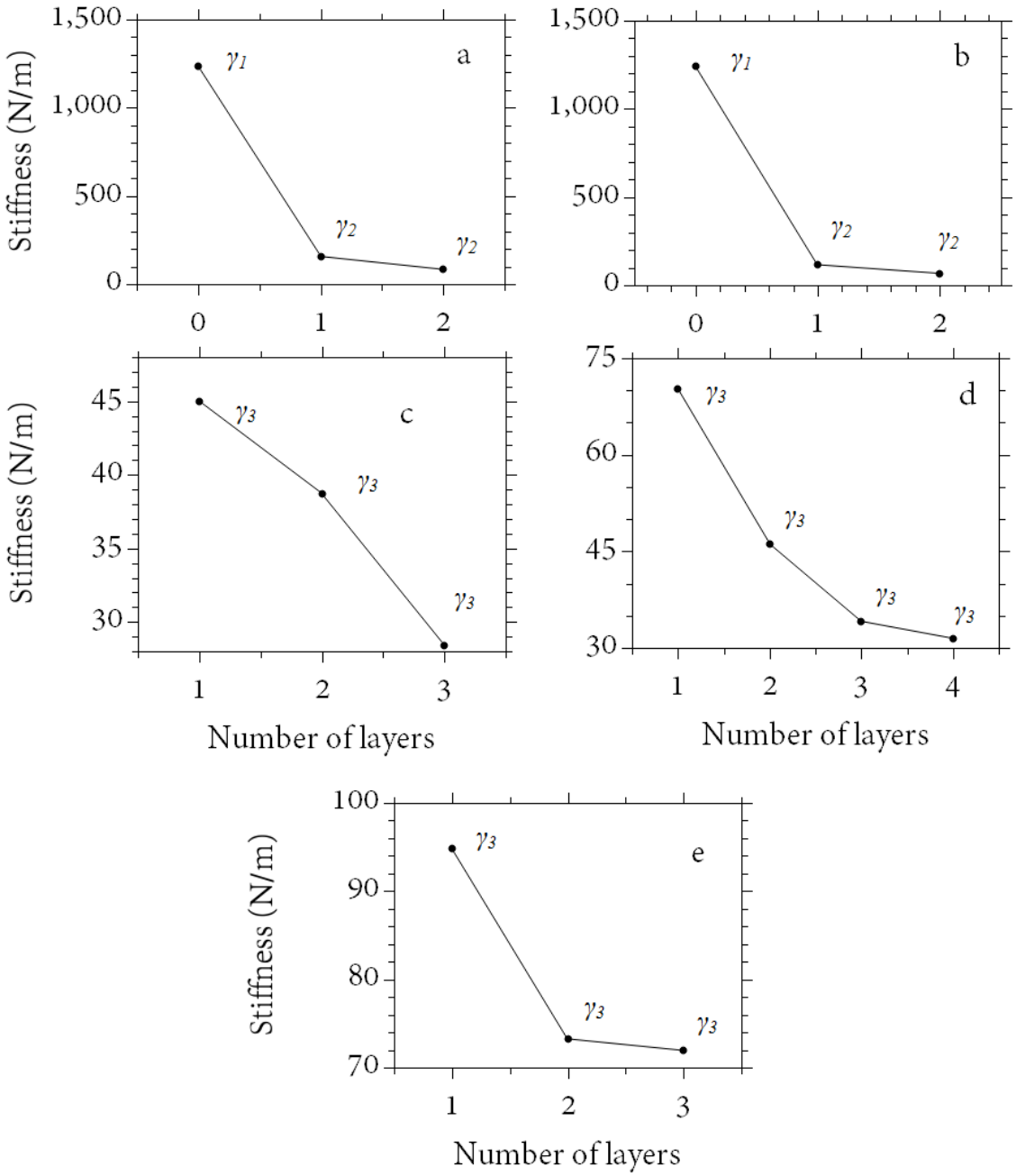

Figure 26: Stiffness variation between SiC-graphene as a function of the number of graphene layers on top of SiC for each hydrogen concentration. Where the letters from a-e respectively denotes the bare SiC in contact with graphene, 30% passivated with H, 60% passivated with H, 100% passivated with H, and finally 100% passivated and covered with H_2 molecules.

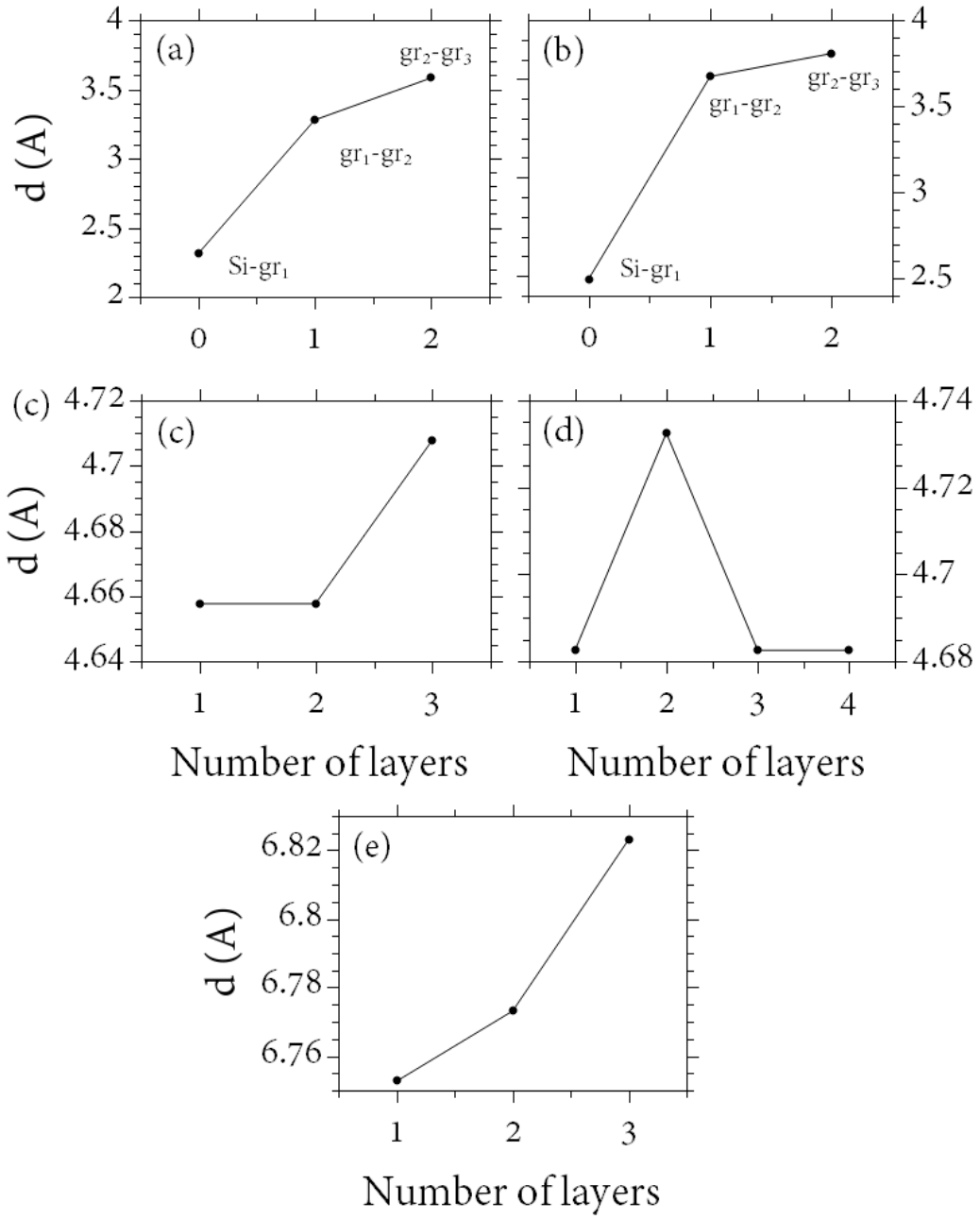

Figure 27: For structures a-e, this figure shows how the minimum energy distance between SiC substrate and the first graphene sheet changes as a function of the number of graphene layers on top of SiC. Where the letters from a-e respectively denotes the bare SiC in contact with graphene, 30% passivated with H, 60% passivated with H, 100% passivated with H, and finally 100% passivated and covered with H_2 molecules.

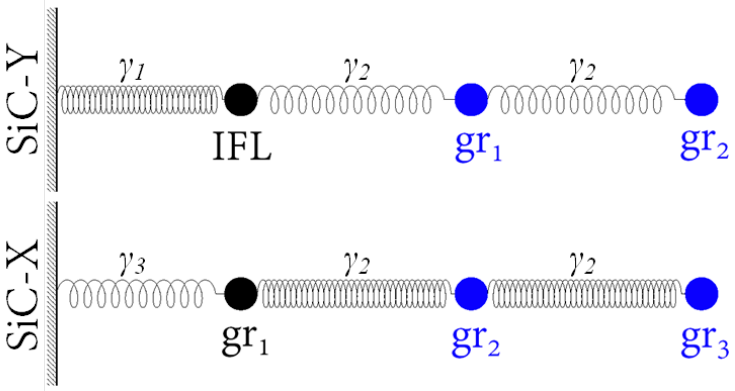

Figure 28: A schematic representation of the force constants, γ_n, govern the stiffness between each two adjacent layers in SiC(Y)-gr_n and SiC(X)-gr_n structures, where n=1, 2, and 3, Y=bare and 4H, and X =8H, 12H, 12H+10H_2. The strength of force constants can be arranged as $\gamma_1 > \gamma_2 > \gamma_3$. The first top scheme represents structures (a) and (b) in Figure 15, and the bottom one illustrates the structures (c), (d), and (e) in Figure 15. One should note that the first graphene layer attached to SiC substrate illustrated in Figure 15(a and b) is an interfacial (IFL) graphene layer and the second layer attached to the IFL graphene is the first graphene layer.

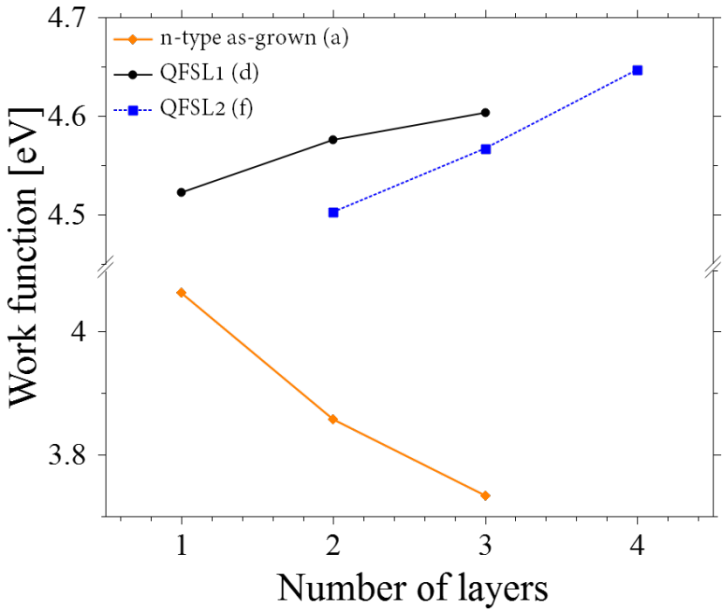

Figure 29: The gradient of work function with number of graphene layers on top of SiC substrate. The letters in the parentheses refer to the unit cells shown in Figure 15. QFSL1 and QFSL2, quasi free standing layers of graphene on top of SiC, respectively refer to bare graphene monolayer and 6.25% passivated with H. These graphene sheets are in contact with SiC with 100% passivated with hydrogen. One should note that as-grown graphene unit cell (a), Figure 15(a), shows interfacial graphene layer on top of SiC substrate, whereas here I have 1-3 layers on top of that interfacial layer.

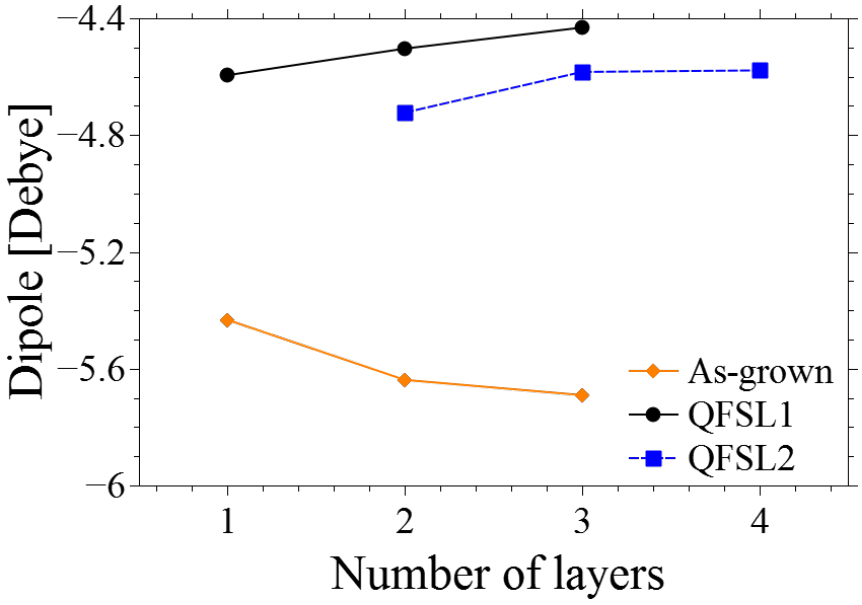

Figure 30: Graphene layer dependence of the electric dipole moment along z direction between the first graphene sheet and the hydrogen terminated end.

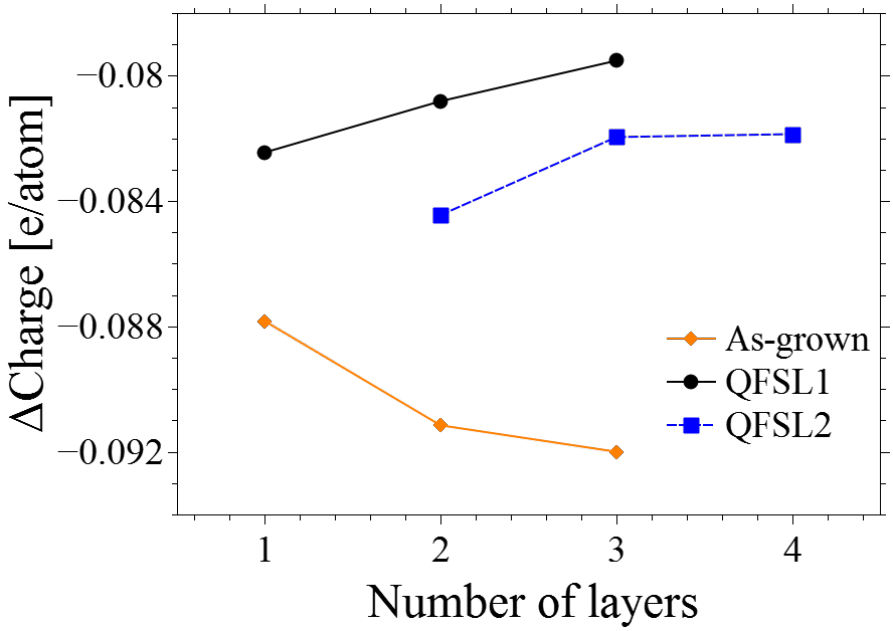

Figure 31: Net charge difference per atom between the first attached graphene layer and the right most hydrogen layer of the unit cells.

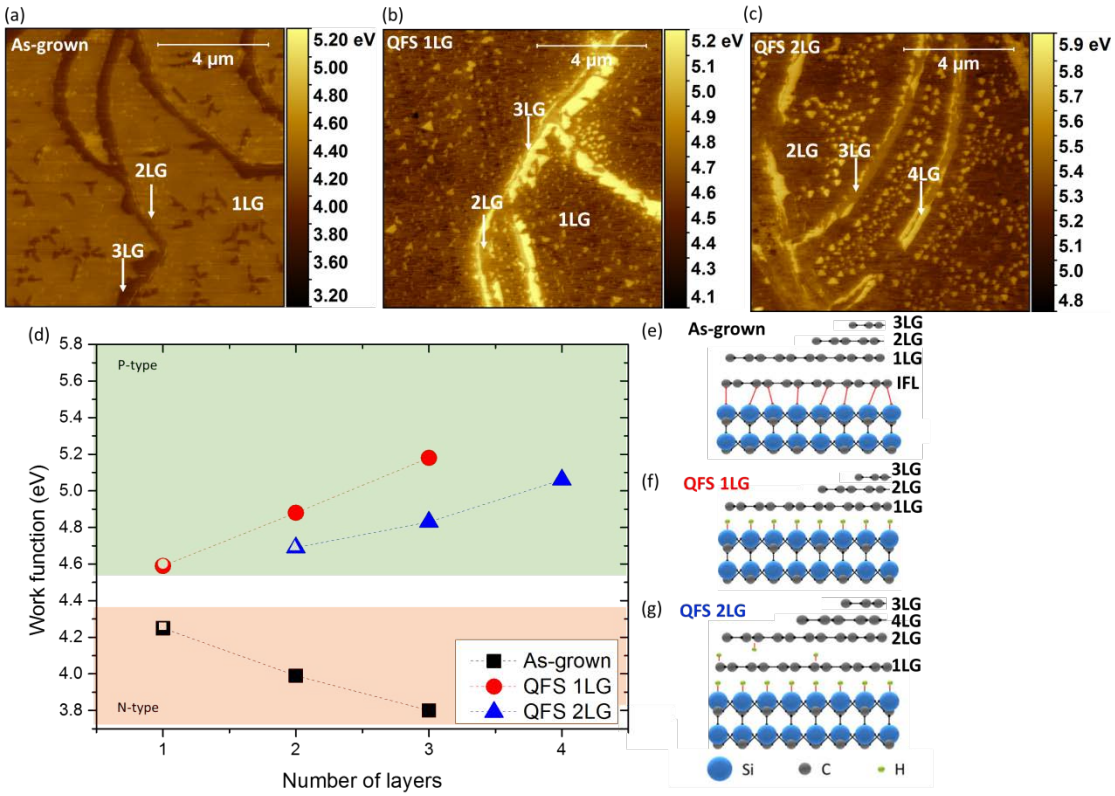

Figure 32: Work function map of: (a) as-grown 1LG showing terraces covered by predominantly 1LG (brightest contrast) and 2LG islands, and terrace edges covered by 2-3LG (darkest contrast). (b) QFSL1 showing terraces covered by predominantly 1LG (darkest contrast) and 2LG islands of triangular shape, and terrace edges covered by 2-3LG (brighter contrast). (c) QFSL2 showing terraces covered by predominantly 2LG (darkest contrast) and 3LG islands, and terrace edges covered by 3-4LG (brighter contrast). (d) Work function summary of all the samples, open/close symbols correspond to measurements done at the terraces/edges, respectively. Sub-figures (e-g) show schematic representation of the layer structure.

4.4. Synopsis

By means of density functional theory, the mechanical properties of silicon-carbide substrate covered with one or multi layers of graphene have been investigated. For these 2-dimensional surfaces, I have studied the correlation between their stiffness and work function on one hand and hydrogen concentration and the number of graphene layers on the other hand. Therefore, I have first modeled the concentration of hydrogen by changing the number of hydrogen atoms intercalating the interface between the top silicon-carbide surface and the directly attached graphene layer. Secondly, I have added more graphene layers on top of the first one to mimic the experimental measurements.

The stiffness of the surface has revealed a number of results, which can be summarid as:

Firstly, the more hydrogen atoms penetrating the interface, the lower the stiffness of the junction. Secondly, the unit cell with approximately 33% of the Si-terminated substrate saturated with hydrogen represents the most stable and stiffest configuration. Further more, there is a threshold limit for hydrogen concentration to detach the graphene from SiC layer underneath. Therefore, I conclude that manipulating the concentration of the H at the interface will eventually determine the electronic and mechanical properties of the junction. Moreover, the stiffness generally possesses three main contributions: the stiffest one is between SiC and the interfacial graphene layer, i.e., a graphene monolayer attached directly to clean or slightly H-doped Si-terminated surface; the softest one is when the concentration of hydrogen is greater than approximately 35% of the surface Si atoms; the final one the stiffness between two adjacent graphene layers. Finaly, the stiffness also decreases with the number of graphene layer.

The work function, as the second property also shows a number of interesting features:

1. The more hydrogen atoms between the layer, the higher the work function.
2. With more hydrogen, the work function approaches the graphene level.
3. SiC surface saturation with approximately 33% with hydrogen breaks the status quo.
4. For the same 2-dimension interface, the higher the dipole at the connection region is, the less work function at the surface will be, regardless of doping.

Chapter 5

Conclusions

In this thesis I have shown that DFT predicts properties which are consistent with experimental measurements through the simulation of two totally distinct problems. The first problem is the thermoelectric properties of a amino-silane functionalized graphene junction. Within this project, Green's function and tight binding methods were also used to tackle the problem. The second implementation of DFT is the calculation of mechanical properties of the interface region of silicon-carbide/graphene junction. The following combined results have emerged from this thesis,

One of the main results emerges from this thesis is that amino-silane molecules can enhance the thermal properties of graphene in electronic devices, and functionalizing graphene with organic molecule improves heat management in the electronic chip.

Another main result is that manipulating hydrogen concentration at the interface between graphene and its substrate can controls the work function, band gap, stiffness, and Fermi level of the junction. Therefore, controlling the concentration leads to better design and effective electronic engineering and that fully hydrogen saturated substrate produces easy to handle graphene. Finally, the threshold level of hydrogen concentration, in my case it is approximately equal to 33%, may have a serious impact on the system properties, which should be scrutinized much more.

In addition, some minor results of the thesis can be also summarised. As a result, the interactions at the graphene-substrate interface effectively control the surface properties. Another result is that an n-type (p-type) system will have higher work function if the number of negative (positive) charges is decreased (increased), provided that the directionality of the dipole is preserved. Moreover, the stiffness of two-dimensional stacked systems is structure-dependent, and cannot be easily inferred due to the fact that the each surface in the multilayer system has different stiffness value, this variation should investigated in depth.

For the future, one can envisage a number of follow on investigations which build upon the above results, inclcuding:

1. How the stiffness is affected by the number of graphene layers.
2. A more detailed analysis about the effect of hydrogen concentration on stiffness and the interface properties.
3. A detailed work function calculation as a function of doping.
4. Testing silane molecules with different leads and junctions.
5. The effect of the concentration level of dopants, such as H or O, at the interface of attached systems on the properties of the junction.

Hopfully I will find an opportunity to tackle these studies in the future year.

Bibliography

1. Novoselov, K.S., et al., *Electric Field Effect in Atomically Thin Carbon Films.* Science, 2004. **306**(5696): p. 666-669.
2. Wei, H. and E. Wang, *Nanomaterials with enzyme-like characteristics (nanozymes): next-generation artificial enzymes.* Chemical Society Reviews, 2013. **42**(14): p. 6060-6093.
3. Melosh, N.A., et al., *Ultrahigh-Density Nanowire Lattices and Circuits.* Science, 2003. **300**(5616): p. 112-115.
4. Das, S., et al., *Designs for Ultra-Tiny, Special-Purpose Nanoelectronic Circuits.* IEEE Transactions on Circuits and Systems I: Regular Papers, 2007. **54**(11): p. 2528-2540.
5. Plimpton, S., *Fast Parallel Algorithms for Short-Range Molecular Dynamics.* Journal of Computational Physics, 1995. **117**(1): p. 1-19.
6. Smith, W. and T.R. Forester, *DL_POLY_2.0: A general-purpose parallel molecular dynamics simulation package.* Journal of Molecular Graphics, 1996. **14**(3): p. 136-141.
7. Emilio, A., et al., *The SIESTA method; developments and applicability.* Journal of Physics: Condensed Matter, 2008. **20**(6): p. 064208.
8. Aviram, A. and M.A. Ratner, *Molecular rectifiers.* Chemical Physics Letters, 1974. **29**(2): p. 277-283.
9. Xiang, D., et al., *Molecular-Scale Electronics: From Concept to Function.* Chemical Reviews, 2016. **116**(7): p. 4318-4440.
10. Sayed, S.Y., et al., *Charge transport in molecular electronic junctions: Compression of the molecular tunnel barrier in the strong coupling regime.* Proceedings of the National Academy of Sciences, 2012. **109**(29): p. 11498-11503.
11. Ferrer, J., et al., *GOLLUM: a next-generation simulation tool for electron, thermal and spin transport.* New Journal of Physics, 2014. **16**(9): p. 093029.
12. José, M.S., et al., *The SIESTA method for ab initio order- N materials simulation.* Journal of Physics: Condensed Matter, 2002. **14**(11): p. 2745.
13. Clark Stewart, J., et al., *First principles methods using CASTEP*, in *Zeitschrift für Kristallographie - Crystalline Materials*. 2005. p. 567.
14. Datta, S., *Electronic transport in mesoscopic systems*. 1995, Cambridge: Cambridge University Press.
15. Mcmurry, S.M., *Quantum Mechanics*. 1996: Prentice Hall. 392
16. Martin, R.M., *Electronic Structure; Basic Theory and Practical Methods*. 2004: Cambridge University Press.
17. Yang, R.G.P.a.W., *Density Functional Theory of Atoms and Molecule*. 1989: Oxford University Press.
18. Kohn, W. and L.J. Sham, *Self-Consistent Equations Including Exchange and Correlation Effects.* Physical Review, 1965. **140**(4A): p. A1133-A1138.
19. Hohenberg, P. and W. Kohn, *Inhomogeneous Electron Gas.* Physical Review, 1964. **136**(3B): p. B864-B871.

20. Hasnip, P.J., et al., *Density functional theory in the solid state.* Philosophical Transactions of the Royal Society of London A: Mathematical, Physical and Engineering Sciences, 2014. **372**(2011).
21. Jones, R.O., *Introduction to Density Functional Theory and Exchange-Correlation Energy Functionals.* NIC Series, 2006. **31**.
22. Jones, R.O. and O. Gunnarsson, *The density functional formalism, its applications and prospects.* Reviews of Modern Physics, 1989. **61**(3): p. 689-746.
23. Artacho, E., et al., *Linear-Scaling ab-initio Calculations for Large and Complex Systems.* physica status solidi (b), 1999. **215**(1): p. 809-817.
24. Ordejón, P., et al., *Unconstrained minimization approach for electronic computations that scales linearly with system size.* Physical Review B, 1993. **48**(19): p. 14646-14649.
25. Junquera, J., et al., *Numerical atomic orbitals for linear-scaling calculations.* Physical Review B, 2001. **64**(23): p. 235111.
26. Sánchez-Portal, D., et al., *Density-functional method for very large systems with LCAO basis sets.* International Journal of Quantum Chemistry, 1997. **65**(5): p. 453-461.
27. Sanvito, S., et al., *General Green's-function formalism for transport calculations with spd Hamiltonians and giant magnetoresistance in Co- and Ni-based magnetic multilayers.* Physical Review B, 1999. **59**(18): p. 11936-11948.
28. Rungger, I. and S. Sanvito, *Algorithm for the construction of self-energies for electronic transport calculations based on singularity elimination and singular value decomposition.* Physical Review B, 2008. **78**(3): p. 035407.
29. Büttiker, M., et al., *Generalized many-channel conductance formula with application to small rings.* Physical Review B, 1985. **31**(10): p. 6207-6215.
30. Cuevas, J.C. and E. Scheer, *Molecular Electronics; An Introduction to Theory and Experiment*. 2010: World Scientific Publishing.
31. Nordholm, S., A. Bäck, and G.B. Bacskay, *The Mechanism of Covalent Bonding: Analysis within the Hückel Model of Electronic Structure.* Journal of Chemical Education, 2007. **84**(7): p. 1201.
32. Yates, K., *Hückel Molecular Orbital Theory*. 1978: ACADEMIC PRESS, INC.
33. Yan, Z., D.L. Nika, and A.A. Balandin *Thermal properties of graphene and few-layer graphene: applications in electronics*. IET Circuits, Devices & Systems, 2015. **9**, 4-12.
34. Geim, A.K. and K.S. Novoselov, *The rise of graphene.* Nat Mater, 2007. **6**(3): p. 183-191.
35. Balandin, A.A., et al., *Superior Thermal Conductivity of Single-Layer Graphene.* Nano Letters, 2008. **8**(3): p. 902-907.
36. Balandin, A.A., *Thermal properties of graphene and nanostructured carbon materials.* Nat Mater, 2011. **10**(8): p. 569-581.
37. Kong, Q.-Q., et al., *Hierarchical Graphene–Carbon Fiber Composite Paper as a Flexible Lateral Heat Spreader.* Advanced Functional Materials, 2014. **24**(27): p. 4222-4228.
38. Yan, Z., et al., *Graphene quilts for thermal management of high-power GaN transistors.* Nat Commun, 2012. **3**: p. 827.

39. Gao, Z., et al., *Thermal chemical vapor deposition grown graphene heat spreader for thermal management of hot spots.* Carbon, 2013. **61**: p. 342-348.
40. Subrina, S., D. Kotchetkov, and A.A. Balandin, *Heat Removal in Silicon-on-Insulator Integrated Circuits With Graphene Lateral Heat Spreaders.* IEEE Electron Device Letters, 2009. **30**(12): p. 1281-1283.
41. Subrina, S., *Modeling Based Design of Graphene Heat Spreaders and Interconnects in 3-D Integrated Circuits.* Journal of Nanoelectronics and Optoelectronics, 2010. **5**(3): p. 281-286.
42. Malekpour, H., et al., *Thermal Conductivity of Graphene Laminate.* Nano Letters, 2014. **14**(9): p. 5155-5161.
43. Prasher, R., *Graphene Spreads the Heat.* Science, 2010. **328**(5975): p. 185.
44. Ong, Z.-Y. and E. Pop, *Effect of substrate modes on thermal transport in supported graphene.* Physical Review B, 2011. **84**(7): p. 075471.
45. Ghosh, S., et al., Nat. Mater., 2010. **9**: p. 555.
46. Sadeghi, M.M., I. Jo, and L. Shi, *Phonon-interface scattering in multilayer graphene on an amorphous support.* Proceedings of the National Academy of Sciences, 2013. **110**(41): p. 16321-16326.
47. Lindsay, L., D.A. Broido, and N. Mingo, *Flexural phonons and thermal transport in graphene.* Physical Review B, 2010. **82**(11): p. 115427.
48. Seol, J.H., et al., *Two-Dimensional Phonon Transport in Supported Graphene.* Science, 2010. **328**(5975): p. 213.
49. Wei, Z., Y. Chen, and C. Dames, *Negative correlation between in-plane bonding strength and cross-plane thermal conductivity in a model layered material.* Applied Physics Letters, 2013. **102**(1): p. 011901.
50. Wang, Z., et al., Nano Lett., 2011. **11**: p. 113.
51. Luo, T. and J.R. Lloyd, *Enhancement of Thermal Energy Transport Across Graphene/Graphite and Polymer Interfaces: A Molecular Dynamics Study.* Advanced Functional Materials, 2012. **22**(12): p. 2495-2502.
52. Hopkins, P.E., et al., *Manipulating Thermal Conductance at Metal–Graphene Contacts via Chemical Functionalization.* Nano Letters, 2012. **12**(2): p. 590-595.
53. Ge, Z., D.G. Cahill, and P.V. Braun, *Thermal Conductance of Hydrophilic and Hydrophobic Interfaces.* Physical Review Letters, 2006. **96**(18): p. 186101.
54. Wang, R.Y., R.A. Segalman, and A. Majumdar, *Room temperature thermal conductance of alkanedithiol self-assembled monolayers.* Applied Physics Letters, 2006. **89**(17): p. 173113.
55. RamanathanT, et al., *Functionalized graphene sheets for polymer nanocomposites.* Nat Nano, 2008. **3**(6): p. 327-331.
56. Konatham, D. and A. Striolo, *Thermal boundary resistance at the graphene-oil interface.* Applied Physics Letters, 2009. **95**(16): p. 163105.
57. Collins, K.C. and G. Chen, Appl. Phys. Lett., 2010. **97**: p. 083102.
58. Liang, Q., et al., *A Three-Dimensional Vertically Aligned Functionalized Multilayer Graphene Architecture: An Approach for Graphene-Based Thermal Interfacial Materials.* ACS Nano, 2011. **5**(3): p. 2392-2401.
59. Ni, Y., et al., *Highly efficient thermal glue for carbon nanotubes based on azide polymers.* Applied Physics Letters, 2012. **100**(19): p. 193118.

60. Harikrishna, H., W.A. Ducker, and S.T. Huxtable, *The influence of interface bonding on thermal transport through solid–liquid interfaces.* Applied Physics Letters, 2013. **102**(25): p. 251606.
61. Liang, Z., et al., *Improvement of heat transfer efficiency at solid-gas interfaces by self-assembled monolayers.* Applied Physics Letters, 2013. **102**(6): p. 061907.
62. O'Brien, P.J., et al., *Bonding-induced thermal conductance enhancement at inorganic heterointerfaces using nanomolecular monolayers.* Nat Mater, 2013. **12**(2): p. 118-122.
63. Taphouse, J.H., et al., *A Pyrenylpropyl Phosphonic Acid Surface Modifier for Mitigating the Thermal Resistance of Carbon Nanotube Contacts.* Advanced Functional Materials, 2014. **24**(4): p. 465-471.
64. Sun, F., et al., *Molecular Bridge Enables Anomalous Enhancement in Thermal Transport across Hard-Soft Material Interfaces.* Advanced Materials, 2014. **26**(35): p. 6093-6099.
65. Chien, S.-K., Y.-T. Yang, and C.o.-K. Chen, *Influence of hydrogen functionalization on thermal conductivity of graphene: Nonequilibrium molecular dynamics simulations.* Applied Physics Letters, 2011. **98**(3): p. 033107.
66. Kim, J.Y., J.-H. Lee, and J.C. Grossman, *Thermal Transport in Functionalized Graphene.* ACS Nano, 2012. **6**(10): p. 9050-9057.
67. Payne, M.C., et al., *Iterative minimization techniques for \textit{ab initio} total-energy calculations: molecular dynamics and conjugate gradients.* Reviews of Modern Physics, 1992. **64**(4): p. 1045-1097.
68. Liu, Y., et al., *Effect of edge-hydrogen passivation and nanometer size on the electronic properties of phagraphene ribbons.* Computational Materials Science, 2016. **117**: p. 279-285.
69. Finch, C.M., V.M. García-Suárez, and C.J. Lambert, *Giant thermopower and figure of merit in single-molecule devices.* Physical Review B, 2009. **79**(3): p. 033405.
70. Claughton, N.R. and C.J. Lambert, *Thermoelectric properties of mesoscopic superconductors.* Physical Review B, 1996. **53**(10): p. 6605-6612.
71. Zeng, M., W. Huang, and G. Liang, *Spin-dependent thermoelectric effects in graphene-based spin valves.* Nanoscale, 2013. **5**(1): p. 200-208.
72. Rejec, T., A. Ramšak, and J.H. Jefferson, *Spin-dependent thermoelectric transport coefficients in near perfect quantum wires.* Physical Review B, 2002. **65**(23): p. 235301.
73. Guttman, G.D., E. Ben-Jacob, and D.J. Bergman, *Thermopower of mesoscopic and disordered systems.* Physical Review B, 1995. **51**(24): p. 17758-17766.
74. Gillemot, K.A., *Quantum control of electrical and thermoelectrical transport in molecular-scale structures*, in *Physics*. 2013, Lancaster.
75. Sivan, U. and Y. Imry, *Multichannel Landauer formula for thermoelectric transport with application to thermopower near the mobility edge.* Physical Review B, 1986. **33**(1): p. 551-558.
76. Hung Nguyen, V., et al., *Enhanced thermoelectric figure of merit in vertical graphene junctions.* Applied Physics Letters, 2014. **105**(13): p. 133105.

77. Hicks, L.D., T.C. Harman, and M.S. Dresselhaus, *Use of quantum-well superlattices to obtain a high figure of merit from nonconventional thermoelectric materials.* Applied Physics Letters, 1993. **63**(23): p. 3230-3232.
78. Widawsky, J.R., et al., *Simultaneous Determination of Conductance and Thermopower of Single Molecule Junctions.* Nano Letters, 2012. **12**(1): p. 354-358.
79. Paulsson, M. and S. Datta, *Thermoelectric effect in molecular electronics.* Physical Review B, 2003. **67**(24): p. 241403.
80. Sharma, A., et al., *van der Waals forces and electron-electron interactions in two strained graphene layers.* Physical Review B, 2014. **89**(23): p. 235425.
81. Schütt, M., *Coulomb Interaction and Transport in Graphene Structures.* 2013, Karlsruher Instituts für Technologie (KIT).
82. de Andres, P.L., R. Ramírez, and J.A. Vergés, *Strong covalent bonding between two graphene layers.* Physical Review B, 2008. **77**(4): p. 045403.
83. Low, T., et al., *Conductance Asymmetry of Graphene p-n Junction.* IEEE Transactions on Electron Devices, 2009. **56**(6): p. 1292-1299.
84. Huard, B., et al., *Transport Measurements Across a Tunable Potential Barrier in Graphene.* Physical Review Letters, 2007. **98**(23): p. 236803.
85. Lambert, C.J., *Basic concepts of quantum interference and electron transport in single-molecule electronics.* Chemical Society Reviews, 2015. **44**(4): p. 875-888.
86. Gómez-Silva, G., et al., *Enhancement of thermoelectric efficiency and violation of the Wiedemann-Franz law due to Fano effect.* Journal of Applied Physics, 2012. **111**(5): p. 053704.
87. Jonson, M. and G.D. Mahan, *Mott's formula for the thermopower and the Wiedemann-Franz law.* Physical Review B, 1980. **21**(10): p. 4223-4229.
88. Kim, T.Y., C.-H. Park, and N. Marzari, *The Electronic Thermal Conductivity of Graphene.* Nano Letters, 2016. **16**(4): p. 2439-2443.
89. d'Honincthun, H.C., et al., *Electron-phonon scattering and ballistic behavior in semiconducting carbon nanotubes.* Applied Physics Letters, 2005. **87**(17): p. 172112.
90. Liu, Y.-S., Y.-R. Chen, and Y.-C. Chen, *Thermoelectric Efficiency in Nanojunctions: A Comparison between Atomic Junctions and Molecular Junctions.* ACS Nano, 2009. **3**(11): p. 3497-3504.
91. Jacquod, P., et al., *Onsager relations in coupled electric, thermoelectric, and spin transport: The tenfold way.* Physical Review B, 2012. **86**(15): p. 155118.
92. Onsager, L., *Reciprocal Relations in Irreversible Processes. II.* Physical Review, 1931. **38**(12): p. 2265-2279.
93. Onsager, L., *Reciprocal Relations in Irreversible Processes. I.* Physical Review, 1931. **37**(4): p. 405-426.
94. Schwierz, F., *Graphene transistors.* Nat Nano, 2010. **5**(7): p. 487-496.
95. Guerriero, E., et al., *Gigahertz Integrated Graphene Ring Oscillators.* ACS Nano, 2013. **7**(6): p. 5588-5594.
96. Han, S.-J., et al., *Graphene radio frequency receiver integrated circuit.* Nature Communications, 2014. **5**: p. 3086.
97. Speck, F., et al., *The quasi-free-standing nature of graphene on H-saturated SiC(0001).* Applied Physics Letters, 2011. **99**(12): p. 122106.

98. Winters, M., et al., *A temperature dependent measurement of the carrier velocity vs. electric field characteristic for as-grown and H-intercalated epitaxial graphene on SiC.* Journal of Applied Physics, 2013. **113**(19): p. 193708.
99. Goler, S., et al., *Revealing the atomic structure of the buffer layer between SiC(0 0 0 1) and epitaxial graphene.* Carbon, 2013. **51**: p. 249-254.
100. Tokarczyk, M., et al., *Structural investigations of hydrogenated epitaxial graphene grown on 4H-SiC (0001).* Applied Physics Letters, 2013. **103**(24): p. 241915.
101. Emtsev, K.V., et al., *Interaction, growth, and ordering of epitaxial graphene on SiC{0001} surfaces: A comparative photoelectron spectroscopy study.* Physical Review B, 2008. **77**(15): p. 155303.
102. Riedl, C., et al., *Quasi-Free-Standing Epitaxial Graphene on SiC Obtained by Hydrogen Intercalation.* Physical Review Letters, 2009. **103**(24): p. 246804.
103. Robinson, J.A., et al., *Epitaxial Graphene Transistors: Enhancing Performance via Hydrogen Intercalation.* Nano Letters, 2011. **11**(9): p. 3875-3880.
104. Melios, C., et al., *Carrier type inversion in quasi-free standing graphene: studies of local electronic and structural properties.* Scientific Reports, 2015. **5**: p. 10505.
105. Lee, C., et al., *Measurement of the Elastic Properties and Intrinsic Strength of Monolayer Graphene.* Science, 2008. **321**(5887): p. 385.
106. Javier, J., H.C. Morrel, and M.R. Karin, *Nanoscale smoothing and the analysis of interfacial charge and dipolar densities.* Journal of Physics: Condensed Matter, 2007. **19**(21): p. 213203.
107. Makov, G. and M.C. Payne, *Periodic boundary conditions in \textit{ab initio} calculations.* Physical Review B, 1995. **51**(7): p. 4014-4022.
108. Bengtsson, L., *Dipole correction for surface supercell calculations.* Physical Review B, 1999. **59**(19): p. 12301-12304.
109. Berland, K. and P. Hyldgaard, *Exchange functional that tests the robustness of the plasmon description of the van der Waals density functional.* Physical Review B, 2014. **89**(3): p. 035412.
110. Kristian, B., et al., *van der Waals forces in density functional theory: a review of the vdW-DF method.* Reports on Progress in Physics, 2015. **78**(6): p. 066501.
111. Engel, E., A. Höck, and R.M. Dreizler, *van der Waals bonds in density-functional theory.* Physical Review A, 2000. **61**(3): p. 032502.
112. Thonhauser, T., et al., *Van der Waals density functional: Self-consistent potential and the nature of the van der Waals bond.* Physical Review B, 2007. **76**(12): p. 125112.
113. Doll, K., *Calculation of the work function with a local basis set.* Surface Science, 2006. **600**(24): p. L321-L325.
114. Djurabekova, F., et al., *Local changes of work function near rough features on Cu surfaces operated under high external electric field.* Journal of Applied Physics, 2013. **114**(24): p. 243302.
115. Jiao, N., et al., *Surface work function of chemically derived graphene: A first-principles study.* Physics Letters A, 2013. **377**(28–30): p. 1760-1765.
116. Junquera, J., et al., *First-principles calculation of the band offset at $BaO/BaTiO_3$ and $SrO/SrTiO_3$ interfaces.* Physical Review B, 2003. **67**(15): p. 155327.

117. Leung, T.C., et al., *Relationship between surface dipole, work function and charge transfer: Some exceptions to an established rule.* Physical Review B, 2003. **68**(19): p. 195408.
118. Li, D.Y. and W. Li, *Electron work function: A parameter sensitive to the adhesion behavior of crystallographic surfaces.* Applied Physics Letters, 2001. **79**(26): p. 4337-4338.
119. Baumgart, F., *Stiffness — an unknown world of mechanical science?* Injury, 2000. **31**: p. 14-84.
120. Herden, T., M. Ternes, and K. Kern, *Lateral and Vertical Stiffness of the Epitaxial h-BN Monolayer on Rh(111).* Nano Letters, 2014. **14**(6): p. 3623-3627.
121. Jadaun, P., et al., *Density functional theory studies of interactions of graphene with its environment: Substrate, gate dielectric and edge effects.* Solid State Communications, 2012. **152**(15): p. 1497-1502.
122. Ohta, T., et al., *Controlling the Electronic Structure of Bilayer Graphene.* Science, 2006. **313**(5789): p. 951.
123. Varchon, F., et al., *Electronic Structure of Epitaxial Graphene Layers on SiC: Effect of the Substrate.* Physical Review Letters, 2007. **99**(12): p. 126805.
124. Xu, Y., et al., *Inducing Electronic Changes in Graphene through Silicon (100) Substrate Modification.* Nano Letters, 2011. **11**(7): p. 2735-2742.
125. Miwa, R.H., W. Orellana, and A. Fazzio, *Substrate-dependent electronic properties of an armchair carbon nanotube adsorbed on H/Si(001).* Applied Physics Letters, 2005. **86**(21): p. 213111.
126. Butler, K.T., et al., *Crystal electron binding energy and surface work function control of tin dioxide.* Physical Review B, 2014. **89**(11): p. 115320.
127. Mattausch, A. and O. Pankratov, *\textit{Ab Initio} Study of Graphene on SiC.* Physical Review Letters, 2007. **99**(7): p. 076802.